The Thesis Committee for Yusuke Inaba
Certifies that this is the approved version of the following Thesis:

Application of commercial FEM program Abaqus to investigate delamination behavior of post-tensioned concrete curved walls

APPROVED BY
SUPERVISING COMMITTEE:

Oguzhan Bayrak, Supervisor

Trevor D. Hrynyk, Co-Supervisor

Application of commercial FEM program Abaqus to investigate delamination behavior of post-tensioned concrete curved walls

by

Yusuke Inaba

Thesis

Presented to the Faculty of the Graduate School of

The University of Texas at Austin

in Partial Fulfillment

of the Requirements

for the Degree of

Master of Science in Engineering

The University of Texas at Austin

August 2020

Dedication

I dedicate this thesis to my family and friends.

Acknowledgements

First of all, I would like to thank those who helped me to make my dream of studying abroad come true. Specifically, I wish to express my sincere appreciation to my supervisor, Dr. Oguzhan Bayrak. I would not have been able to complete my research without his valuable and thoughtful guidance. I will never forget that he constantly encouraged me and gave me kind support even in the difficult situation of COVID-19 pandemic. I also wish to express my gratitude to my co-supervisor, Dr. Trevor D. Hrynyk. He gave me a lot of insightful advice, especially on the numerical analysis part of my research. I firmly believe that his instruction has made my research fruitful.

I gratefully acknowledge the support provided by KAJIMA CORPORATION through their employee scholarship program.

My sincere appreciation also needs to be expressed to all the wonderful professors, researchers, students, and staff members at the Ferguson Structural Engineering Laboratory. In particular, I wish to extend my thanks to Dr. Juan Murcia-Delso. His input has helped me to make significant progress in my research. Furthermore, I am grateful to Dr. Jongkwon Choi for his help. He has kindly shared his insights into the wall delamination test and given me a variety of advice on student life in Austin.

Lastly, I would like to express my heartfelt appreciation to my parents and friends in Japan. Even though they were far away, they supported me in so many ways. Thank you.

Abstract

Application of commercial FEM program Abaqus to investigate delamination behavior of post-tensioned concrete curved walls

Yusuke Inaba, M.S.E

The University of Texas at Austin, 2020

Supervisor: Oguzhan Bayrak

Co-Supervisor: Trevor D. Hrynyk

The concrete delamination induced by prestressing forces is a potential problem of post-tensioned concrete containments with curved geometry. To investigate the concrete delamination mechanism, the researchers of the University of Texas at Austin completed an experimental research project in 2017. In this research project, the academic finite element method (FEM) program VecTor4, which has powerful shell-type elements for cracked reinforced concrete shells, was modified and proved to be an appropriate tool to predict the level of applied prestressing load at the delamination failure.

VecTor4 has a well-defined reinforced concrete material model and capability to analyze the structures on an overall system level with low computational resources. However, its user interface has limitations, and the details of the local behavior of structures may not be captured due to its simplicity. On the other hand, commercial FEM programs generally provide a convenient graphical-based user interface and various analysis features. Still, typical commercial FEM programs are not designed to analyze the

concrete structures. Some commercial FEM programs provide concrete material models; however, they tend to require significant calibration analyses to capture the behavior of reinforced concrete structures. Specifically, to capture the delamination of concrete walls with those programs, solid elements should be selected, which should increase the computational costs. However, commercial FEM programs can potentially provide the details of the local behavior of structures.

Recently, an experimental test investigating the concrete delamination phenomenon was conducted. In this recent test, numerical analyses with the commercial FEM program Abaqus ware conducted as well as the analysis with VecTor4 to explore other options in commercial FEM programs. This paper will show the analysis results of both Abaqus and VecTor4 for the recent test. Additionally, the discussion on the relative merits and limitations of these programs obtained from the experience of the analyses for the recent test is presented.

Table of Contents

List of Tables

List of Figures

Chapter 1. Introduction

Nuclear containments are required to maintain the structural integrity and function as a barrier preventing the leakage of radioactive particles from internal components under different possible scenarios. The post-tensioned prestressed concrete structure has been widely adopted to nuclear containments over the past decades as it can show high performance against extreme loads such as the internal pressure caused by severe nuclear accidents.

Prestressed concrete techniques can increase the resistance against tensile stresses of a containment structure subjected to internal pressure by enforcing in-plane compression forces through tendons embedded in concrete. However, accompanying the in-plane compression forces, out-of-plane normal stresses generate in a prestressed concrete curved structure due to the curved profile of tendons (see Figure 1.1). Excessive out-of-plane stresses can result in the cracks, or even worse, cause wall delamination failure.

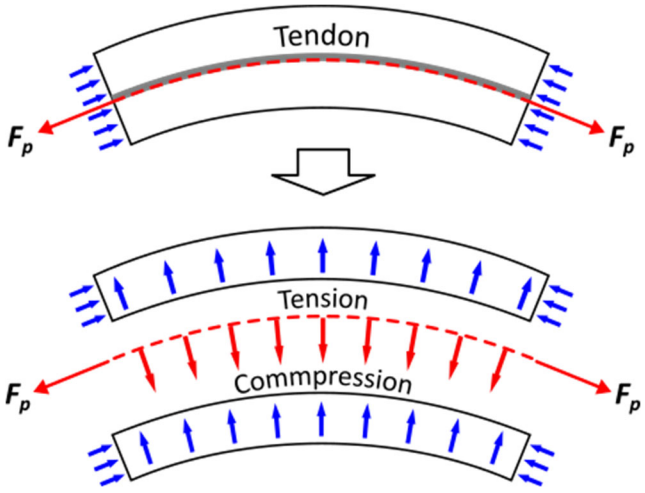

Figure 1.1: Out-of-plane stress induced by prestressing force in post-tensioned concrete curved structure (adapted from Choi et al., 2017)

This chapter will provide a brief overview of the past research on the delamination behavior of post-tensioned concrete curved shells and discuss the research significance of the present study.

1.1. BACKGROUND

The concrete delamination in the wall section of nuclear containment was first found at the Crystal River Nuclear Power Plant Unit-3 in Florida during the construction of an additional opening in 2009 (NEA-CSNI, 2015). Several incidents of the similar concrete delamination in the dome sections of nuclear containment structures had also been reported since the 1970s (Florida Power and Light Company, 1970; Florida Power Corporation, 1976; Basu and Gupchup, 2004) (see Figure 1.2). These incidents motivated researchers to investigate the root cause of the delamination phenomenon in post-tensioned concrete curved structures (Acharya and Menon, 2003; Wang and Munshi, 2012; Bae 2013; Wang and Munshi, 2013), and the provisions in the code for out-of-plane reinforcement were revised (ASME, 2015). However, none of the experimental research focusing on the out-of-plane stresses had been done for decades (Choi et al., 2017; Choi, 2018).

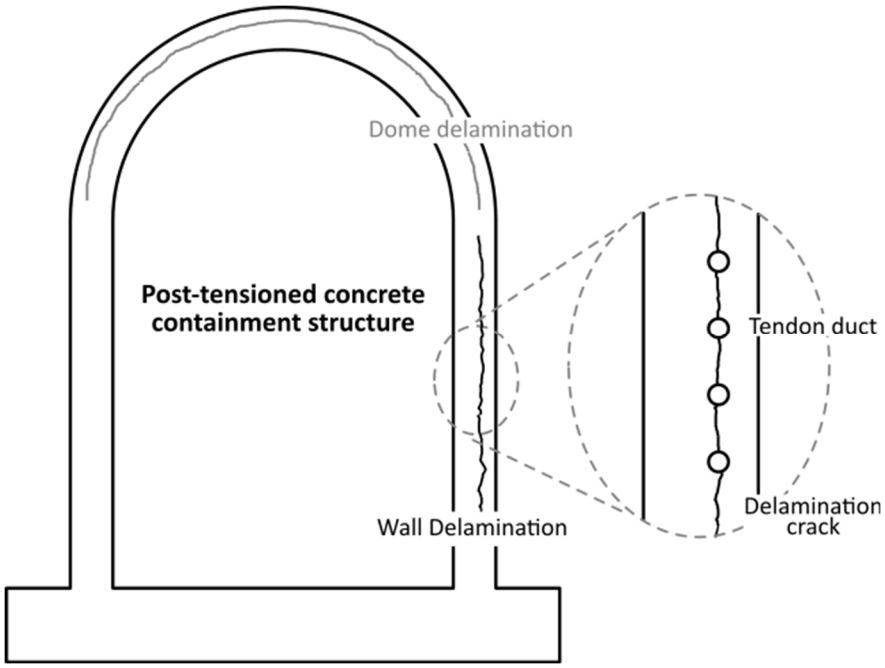

Figure 1.2: Delamination crack in a post-tensioned concrete containment structure

A series of experimental tests had been conducted by researchers at the University of Texas at Austin to improve the understanding of the delamination behavior of post-tensioned concrete curved structures (Choi et al., 2017; Choi, 2018, Choi et al., 2020). In the research project, three post-tensioned curved wall specimens were designed and constructed to investigate the effect of the specimen size and the maximum aggregate size on the mechanism of concrete delamination. The tests revealed that the specimen size and the maximum aggregate size affect the delamination cracking as well as the delamination failure load. Additionally, it was found that the circumferential compressive stress level at the first delamination crack was considerably lower than the service stress limit of $0.35f_c'$ specified in the ASME BPVC (ASME, 2015; Choi, 2018). In the same research project, an analytical study was also conducted using noncommercial nonlinear finite element analysis program (NLFEA), VecTor4, which employs layered shell finite elements to model

reinforced concrete shell structures. The VecTor4 program was modified to accommodate out-of-plane normal stress distributions of post-tensioned concrete curved shells properly, and the analysis results demonstrated that the modified VecTor4 program could predict the general trend of the delamination behavior of post-tensioned curved walls with high efficiency.

1.2. MOTIVATION

FEM is a powerful technique for solving complex problems to evaluate the behavior of structures and may provide further insights into structural tests if it is appropriately used. In this regard, the modified VecTor4 program was proved to be an efficient tool to evaluate and understand the wall delamination in the previous research. VecTor4 is equipped with a well-defined reinforced concrete material model and has the capability to analyze the structures on an overall system level with low computational resources. However, its pre- and post- processors have limitations, and the details of the local behavior of structures may not be captured due to its simplicity. On the other hand, commercial FEM programs generally provide a convenient graphical-based user interface and various analysis features. However, typical commercial FEM programs are not designed to analyze the concrete structures. Though some commercial FEM programs provide concrete material models, those models tend to require a lot of calibration analyses to capture the behavior of reinforced concrete structures subjected to complicated load conditions. Further, to capture the delamination of concrete walls with those programs, solid elements should be selected, which also increases the computational costs. However, commercial FEM programs can potentially provide the details of the local behavior of structures.

Recently, a supplemental test for the concrete delamination was completed at the University of Texas at Austin to investigate the influence of tendon spacings. Regarding the analytical study, the commercial program Abaqus was employed as the potential alternative option to analyze the wall delamination. The analysis with Abaqus was attempted in addition to the investigation with the modified version of VecTor4.

This thesis primarily aims to provide the relative merits and limitations of Abaqus and the modified VecTor4 obtained from the experience of the analyses for the recent test. In the next section, the latest experimental test of the post-tensioned concrete curved wall is briefly summarized. Then, nonlinear finite element analyses for the test with both Abaqus and VecTor4 are shown. Finally, the discussion focusing on the validity, and the computational cost are presented.

Chapter 2. Summary of Recent Test

The recent test was conducted as an additional test to the previous series of tests for a better understanding of the delamination behavior of post-tensioned concrete curved walls. The test was primarily aimed to investigate the influence of the tendon spacing on the delamination behavior. This section provides a summary of the recent test: further details and discussion were reported by Choi (2020).

2.1. TEST SPECIMEN

The test specimen was a 90-degree post-tensioned concrete curved wall representing a cylindrical concrete structure (see Figure 2.1). The curved wall section was mainly designed following the requirement of ACI 318-14 and ASME BPVC Section III, Division 2 (ACI Committee 318, 2014; ASME, 2015). The mild reinforcing bars were provided with a ratio of 0.40 % in the interior and exterior surface of the specimen in the circumferential direction. The nominal reinforcement ratio in the vertical direction was 0.28 % on both surfaces. The wall was constructed without through-thickness (radial) reinforcement. The live-end and dead-end anchor blocks were designed sufficiently rigid to avoid their failure during the test. Two ducts of tendons were placed on the line slightly shifted from the exact center of the wall section due to the eccentricity of the strands in each duct (see Figure 2.1). In this manner, the strands were deemed to be at the centerline of the wall during the test. These ducts were distributed evenly in the vertical direction. The curved galvanized steel tubes with a 14-gauge thickness (0.085 in. [2.16 mm]), of which outer diameter was 4.0 in. (102 mm), was adopted for the tendon ducts. Each duct contained 19 strands with a diameter of 0.6 in. (15 mm).

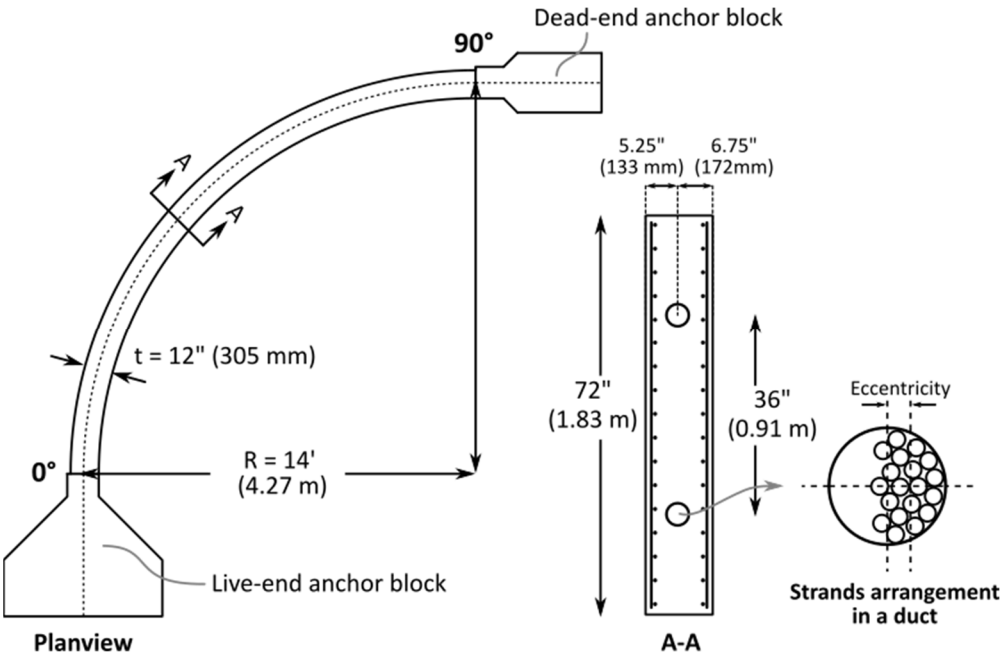

Figure 2.1: Test specimen

The material properties of the test specimen are summarized in Table 2.1. The compressive strength was measured from concrete cores after the test. Direct tensile testing was used to determine the tensile strength. The maximum coarse aggregate size was 1.0 in. (25.4 mm). Regarding the Grade 60 No.4 reinforcing bars, the mechanical properties shown in the table are based on the test report from the reinforcing bar supplier. Material properties of Grade 270 seven-wire strands are also shown in the same table.

Table 2.1: Material properties

Concrete	Compressive strength f_c', ksi (MPa)	6.65 (45.9)
	Compressive secant modulus E_{cs}, ksi (MPa)	4,760 (32,840)
	Direct tensile strength f_t', psi (MPa)	388 (2.68)
No.4 Reinforcing bar	Yield stress f_y, ksi (MPa)	63.0 (434)
	Ultimate strength f_u, ksi (MPa)	92.0 (634)
	Elastic modulus* E_s, ksi (MPa)	29,000 (200,000)
0.6 in. (15 mm) Seven wire strands	Ultimate strength f_u, ksi (MPa)	285 (1,965)
	Elastic modulus E_s, ksi (MPa)	29,000 (199,950)

* The typical value was assumed for the elastic modulus of reinforcing bars.

Instrumentations were densely placed at 15-degree, and 45-degree locations as the delamination was expected to form around 15-degree from the live-end anchor block. Linear strain conversion transducers (LSCTs) were installed at 9-, 15-, 21-, 33-, and 45-degree locations to measure through-thickness (radial) expansions of the curved wall during the testing. The strain gages were attached to both circumferential and vertical reinforcing bars at 15- and 45-degree location. Embedded concrete strain gages were installed in the radial direction at 15- and 45-degree. Concrete surface strain gages were placed at the 15- and 45-degree location.

2.2 Test Setup and Loading Protocol

The overview of the test setup is depicted in Figure 2.2. The live-end anchor block was fixed to the laboratory floor. The polytetrafluoroethylene (PTFE) sheets were placed under the curved wall and the dead-end anchor block to mitigate the friction between the specimen and the wooden base. In this way, the specimen could be statically determinate during the structural test. A steel plate that was 10-in. (254-mm) thick served as a stressing plate and was placed in front of the live-end anchor block. Four 800 kips (3560 kN) rams were mounted on the live-end anchor block. Those rams pushed the stressing plate away from the live-end anchor block so as to apply the prestressing loads on the strands.

The prestressing loads were applied monotonically to the specimen during the test. However, the loading was stopped before its failure due to an unexpected rotation of the stressing plate, and the specimen was unloaded. After thorough inspection and realignment of the stressing plate, the specimen was loaded again until delamination failure occurred. The total applied load was 1460 kips (6496 kN), and failure occurred in a brittle manner.

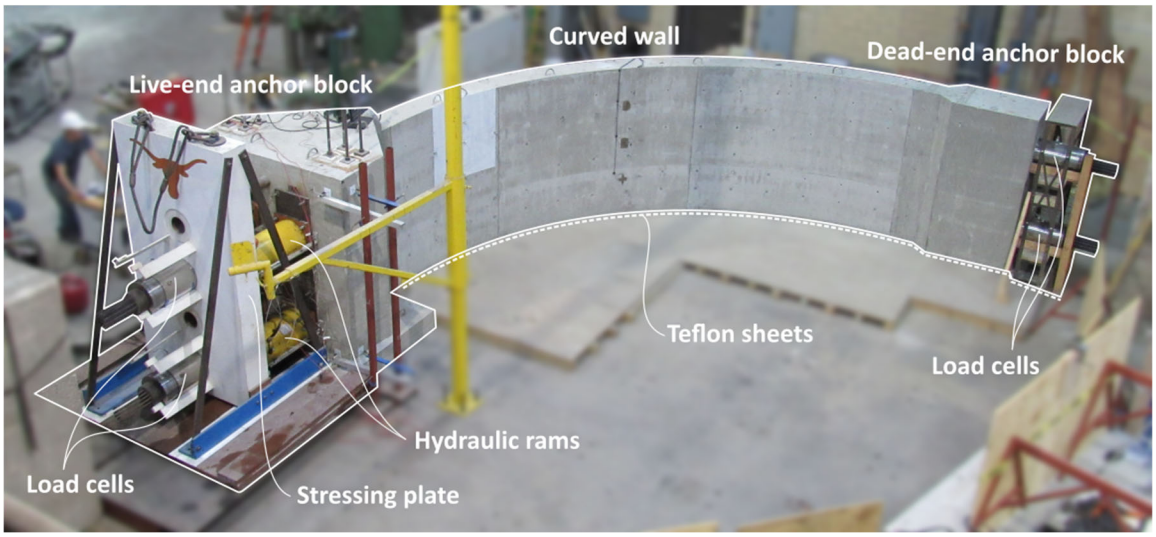

Figure 2.2: Test setup

2.3 Visual Inspection and Test Result

The expected behavior modes of the test specimen are summarized in Figure 2.3. The global bending moment and the buckling of the wall are grouped as a global behavior. The behaviors induced by shear force and bending moment over the height of the specimen were considered as a sectional behavior, and the delamination cracking near the ducts was thought to be a local behavior. (Choi, 2018, Choi et al., 2020).

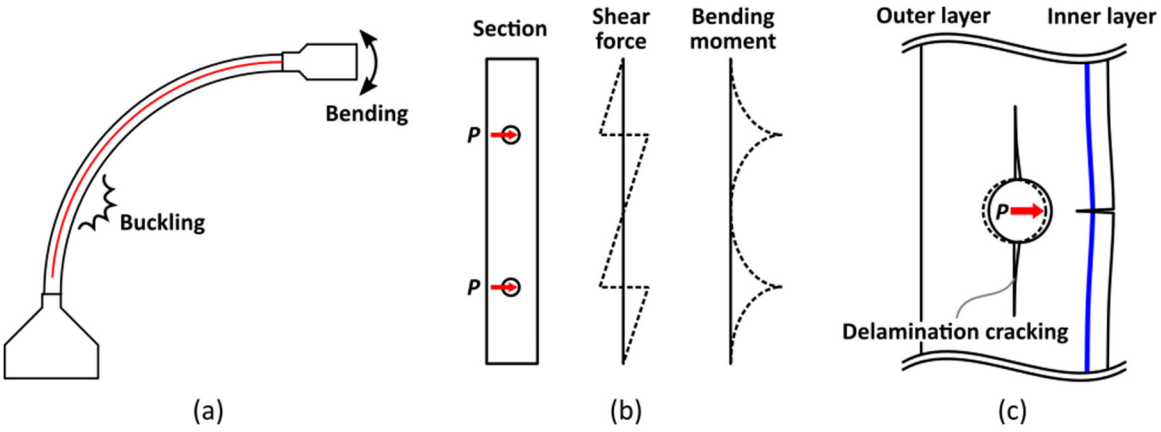

Figure 2.3: Specimen behavior due to prestressing load: (a) global behavior; (b) sectional behavior; and (c) local behavior. (reproduced from Choi 2018)

Figure 2.4 shows the crack patterns of the specimen after the delamination failure. The red lines in Figure 2.4 (a) represent the horizontal surface cracks formed along the duct elevation, which are likely induced by the sectional bending moment over the height of the section due to the prestressing load. As shown in Figure 2.4 (b), the extent of delamination crack was observed from 0 to 60 degrees from the live-end anchor block. The inclined delamination crack pattern was found in the sectional view at 15-degree (see Figure 2.4 (c)).

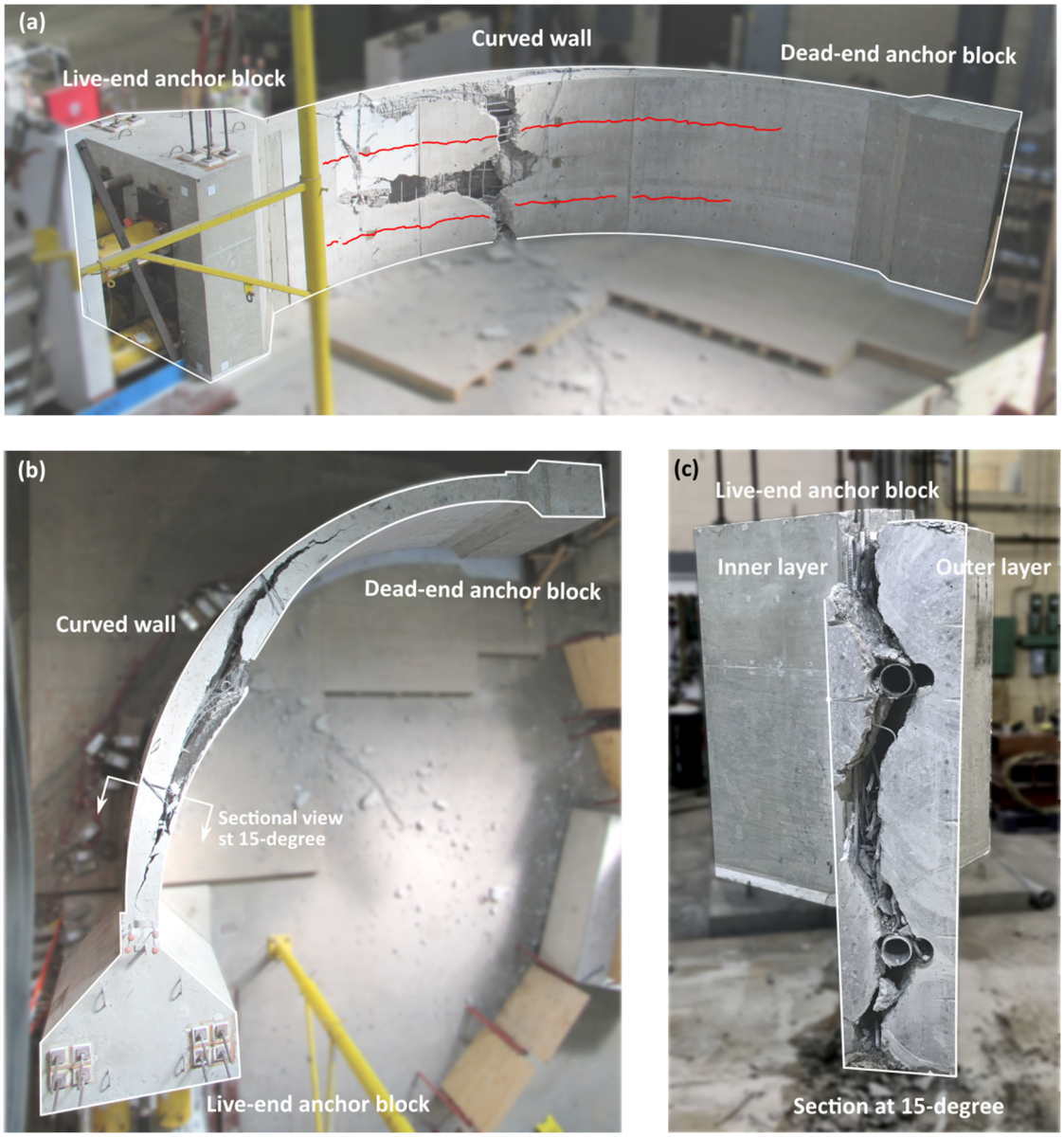

Figure 2.4: Crack patterns of specimen after delamination failure: (a) front-view; (b) top-view; and (c) sectional view at 15-degree location

Through-thickness wall expansion is one of the most critical indicators of wall delamination. The applied prestressing load versus radial expansion data of the section at 9-degree, 15-degree, 21-degree, and 33-degree at the height of the upper tendon are compared, as shown in Figure 2.5. The expansion data at 9-degree location shows the most considerable deformation at the peak load among the radial expansion data at the height of the upper tendon. On the other hand, the data-at 33-degree location implies the smallest deformation. It is deemed that this is because the prestressing load should reduce from the live-end to the dead-end due to friction loss in the tendon, which should affect the radial stress. The through-thickness expansion data at the 9-degree, 15-degree, and 21-degree locations were selected to validate the analysis results shown in the later section because these locations are considered to be more critical than the 33-degree location due to the friction losses of the prestressing forces.

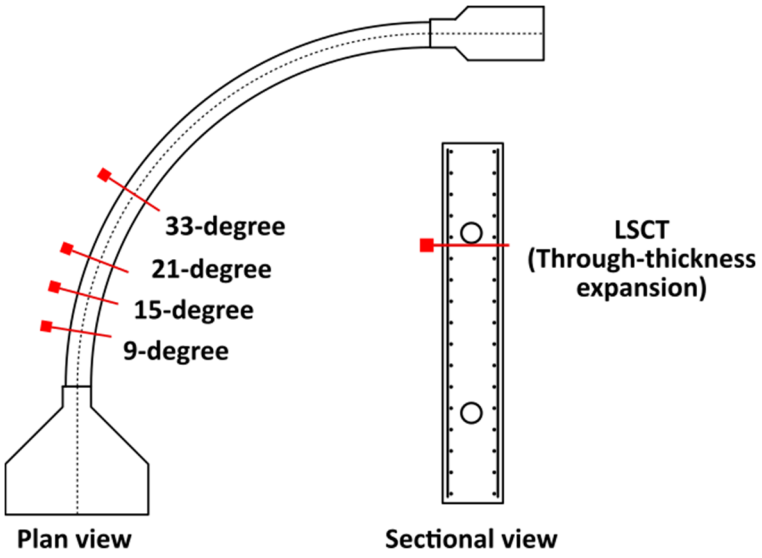

(a)

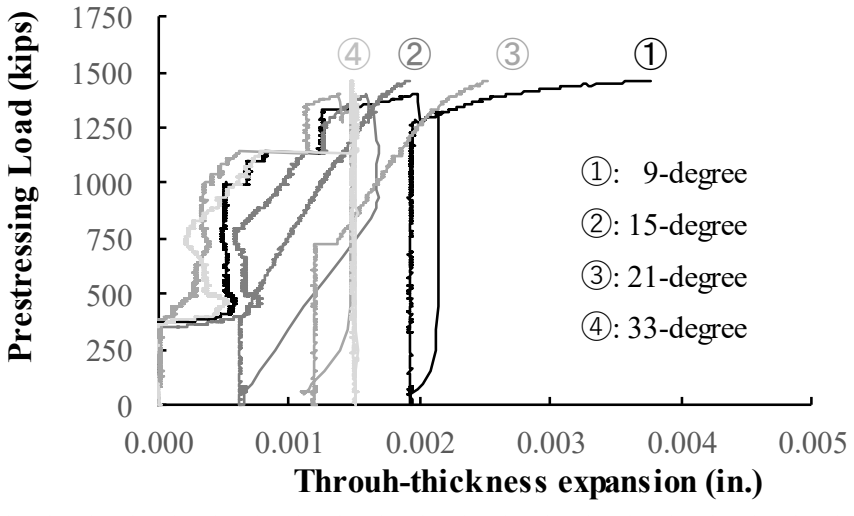

(b)

Figure 2.5: Through-thickness expansions at the height of upper tendon: (a) locations of measurement shown in (b); and (b) comparison of the data at each location

The applied prestressing load versus the circumferential strain on the inner surface of the concrete wall ware compared at the locations of 15-degree and 45-degree in Figure 2.6. It should be mentioned that the circumferential strain data shown in the figure were averaged over the height of the specimen at each section. The circumferential strain at the 15-degree location is larger than that of the 45-degree location, which implies that the larger prestressing loads ware applied on the 15-degree than the 45-degree location. These data also will be used to validate the analysis results in the later section.

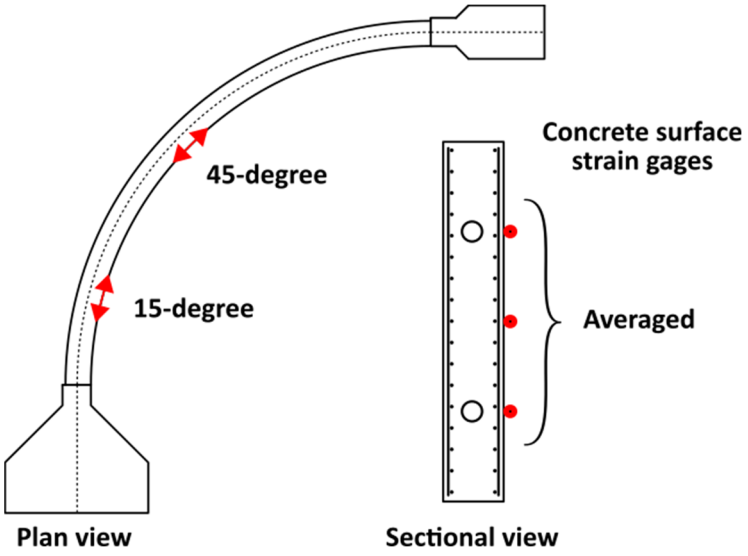

(a)

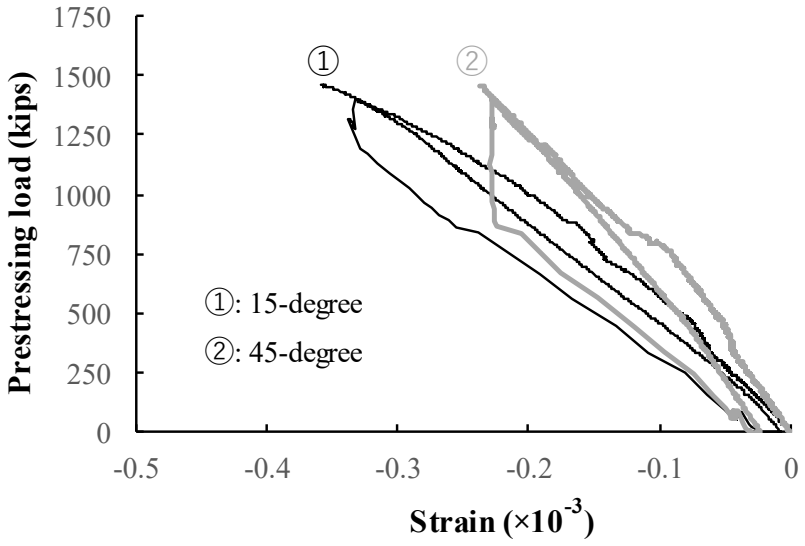

(b)

Figure 2.6: Circumferential strain on the inner surface of the concrete wall: (a) locations of measurement shown in (b); and (b) comparison of the data at each location

Chapter 3. Nonlinear Finite Element Analysis

A series of nonlinear FEM analyses were performed to investigate the relative merits of a commercial FEM program and the academic program, VecTor4. For commercial software, Abaqus was chosen because it is one of the most widely used multi-purpose FEM programs, which is equipped with nonlinear material models for concrete. VecTor4 is an academic FEM program specialized in reinforced concrete structures and already validated to be capable of capturing for the delamination behavior of the post-tensioned concrete curved walls in the past studies conducted by Choi (2018).

This chapter will present a brief overview of the FEM programs employed in this thesis, and the analysis results for the recent test using each program.

3.1 ABAQUS

Abaqus is a commercial FEM program widely used in both academia and industry for the purpose of detailed behavioral analysis, evaluation, and design for various structures. To investigate the performance of Abaqus on analyzing the delamination behavior of the post-tensioned concrete curved walls, Abaqus 3DEXPERIENCE R2017x was employed.

Abaqus provides both implicit and explicit solver. The subsequent analyses were conducted with the implicit solver called Abaqus/Standard, which is necessary for quasi-static/monotonic analyses. It is also worth noting that an efficient parallel computing scheme of Abaqus allows users to perform large-scale model analysis in reasonable computing time with its implicit solver.

3.1.1 Concrete Damaged Plasticity Model (CDPM)

For concrete material modeling, Abaqus/Standard offers two material models: the concrete smeared cracking model, and the concrete damaged plasticity model (CDPM). The concrete smeared cracking model is designed for the concrete with low confining pressures subjected to monotonic loadings. On the other hand, the CDPM can be suitable for more general loading conditions, including cyclic and dynamic loadings; hence the CDPM was adopted in the subsequent analyses with Abaqus (Dassault Systemes Simulia Corp, 2017). The CDPM in Abaqus is based on the plasticity theory coupled with the damage mechanics proposed by Lubliner et al. (1989) and modified by Lee and Fenves (1998). This subsection provides a brief overview of the CDPM to contrast the adopted material models of Abaqus and VecTor4.

The constitutive models of the classical plasticity theory can be characterized by a yield function, a hardening law, and a flow rule. A yield function describes the state of materials by limiting the domain of stresses in which the material can be considered as elastic (Souza Neto et al., 2008). Its boundary is termed with a yield surface. A hardening law controls the evolution of a yield surface with hardening variables. A flow rule defines the development of plastic strains. The plasticity theory generally assumes that the total strain rate $\dot{\varepsilon}$ can be decomposed into the sum of the elastic strain rate $\dot{\varepsilon}^{el}$ and the plastic strain rate $\dot{\varepsilon}^{pl}$. The elastic response can be determined by generalized Hooke's law (Chen, 1982).

In the CDPM, the elastic response of the material is determined considering the degradation of elastic modulus induced by damage of cracked concrete as described below:

.

$$\boldsymbol{\sigma} = (1 - d)\boldsymbol{D}_0^{el}\colon(\varepsilon - \varepsilon^{pl}) = \boldsymbol{D}^{el}\colon(\varepsilon - \varepsilon^{pl}), \qquad \text{Equation 3-1}$$

where d is the scalar stiffness degradation variable; $\boldsymbol{D}_0^{el}$ is initial elastic modulus; and $\boldsymbol{D}^{el}$ is degraded elastic modulus. The variable d represents the ratio of the damaged area to the overall cross-sectional area of the material. It takes values ranging from zero to one.

The CDPM is described in terms of effective stress. The effective stress $\overline{\boldsymbol{\sigma}}$ is the representative value of stress virtually acting on the undamaged load-carrying area, which is defined as,

$$\overline{\boldsymbol{\sigma}} \overset{\text{def}}{=} \boldsymbol{D}_0^{el} : (\varepsilon - \varepsilon^{pl}). \qquad \text{Equation 3-2}$$

In the CDPM in Abaqus, the equivalent plastic strains in tension $\tilde{\varepsilon}_t^{pl}$ and compression $\tilde{\varepsilon}_c^{pl}$ are defined as hardening variables. These variables involve the dissipation of the fracture energy of the material. They are given by the form

$$\tilde{\boldsymbol{\varepsilon}}^{pl} = \begin{bmatrix} \tilde{\varepsilon}_t^{pl} \\ \tilde{\varepsilon}_c^{pl} \end{bmatrix}. \qquad \text{Equation 3-3}$$

The yield function is described in terms of the effective stress and the hardening variables, as shown below:

$$F(\overline{\boldsymbol{\sigma}}, \tilde{\varepsilon}^{pl}) \leq 0. \qquad \text{Equation 3-4}$$

The specific form of the yield function in Abaqus (see Equation 3-5) was initially proposed by Lubliner et al. (1988) and modified by Lee and Fenves (1998).

$$F = \frac{1}{\alpha}(\bar{q} - 3\alpha\bar{p} + \beta(\tilde{\boldsymbol{\varepsilon}}^{pl})\langle\hat{\bar{\sigma}}_{max}\rangle - \gamma\langle-\hat{\bar{\sigma}}_{max}\rangle) - \bar{\sigma}_c(\tilde{\boldsymbol{\varepsilon}}^{pl}) = 0,$$

Equation 3-5

where $\hat{\bar{\sigma}}_{max}$ is the maximum principal effective stress, $\bar{p}$ is the hydrostatic pressure stress, and $\bar{q}$ is the Mises equivalent stress. The values of α, β, and γ in the Equation 3-5 are calculated with the following formulas.

$$\alpha = \frac{(\sigma_{b0}/\sigma_{c0}) - 1}{2(\sigma_{b0}/\sigma_{c0}) - 1};\ 0 \le \alpha \le 0.5, \qquad \text{Equation 3-6}$$

$$\beta = \frac{\bar{\sigma}_c\left(\tilde{\varepsilon}_c^{pl}\right)}{\bar{\sigma}_t\left(\tilde{\varepsilon}_t^{pl}\right)}(1-\alpha) - (1+\alpha), \qquad \text{Equation 3-7}$$

$$\gamma = \frac{3(1-K_c)}{2K_c - 1}, \qquad \text{Equation 3-8}$$

where $\sigma_{b0/}\sigma_{c0}$ is the ratio of the biaxial compressive yield stress to uniaxial compressive yield stress, $\bar{\sigma}_c\left(\tilde{\varepsilon}_c^{pl}\right)$ is the effective compressive cohesion stress, and $\bar{\sigma}_t\left(\tilde{\varepsilon}_t^{pl}\right)$ is the effective tensile cohesion stress. The shape factor K_c in Equation 3-8 determines the shape of the yield surface.

Many of the plasticity models for soils, rocks, and concrete, including the CDPM, employ the non-associated flow rule to account for the dilatancy effect of those materials. In the non-associated flow rule, the plastic strain evolves normal to the plastic potential surface, which has a different shape from the yield surface. The flow rule is described as

$$\dot{\varepsilon}^{pl} = \dot{\lambda}\frac{\partial G(\bar{\boldsymbol{\sigma}})}{\partial \bar{\boldsymbol{\sigma}}}, \qquad \text{Equation 3-9}$$

where $\dot{\lambda}$ is the nonnegative plastic multiplier; and $G(\bar{\boldsymbol{\sigma}})$ is the plastic potential function. The CDPM in Abaqus adopts the Drucker-Prager hyperbolic function as a plastic potential function, as shown below.

$$G = \sqrt{\epsilon\sigma_{t0}\tan\psi + \bar{q}^2} - \bar{p}\tan\psi, \qquad \text{Equation 3-10}$$

where ψ is the dilation angle of plastic potential function measured in the $\bar{p}$-$\bar{q}$ plane at high confining pressure; σ_{t0} is the uniaxial tensile stress at failure, and ϵ is the eccentricity parameter (see Figure 3.1). Due to the adoption of the non-associated flow rule, the CDPM requires the solution of nonsymmetric equations.

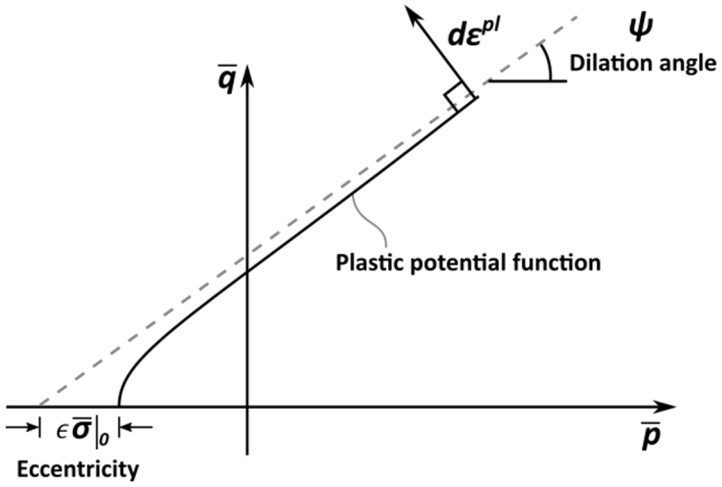

Figure 3.1: Plastic potential function (reproduced from Dassault Systemes Simulia Corp, 2017)

Additionally, Abaqus provides the function called the viscoplastic regularization of the constitutive equations to reduce the convergence difficulties induced by the material softening. The convergence of the implicit solutions can be more difficult when the material model shows severe softening responses. This function helps the tangent stiffness of the materials in the softening regime to be positive. A sufficiently small value of the viscosity parameter μ relative to the time increment of the analysis for the viscoplastic regularization can improve the convergence rate without the undesirable impact on the analysis results (Dassault Systemes Simulia Corp, 2017).

3.1.2. Modeling of Curved Wall Specimen

3.1.2.1 Parameters for Material Models

The recent test specimen showed the inclined cracks in its section (see Figure 2.4 (c)), which implies that the specimen experienced severe local shear induced by the prestressing loads. Therefore, the parameters for the CDPM were calibrated primarily based on the analytical studies on the punching shear failure of the concrete slabs with Abaqus conducted by Genikomsou (2015).

For the CDPM, users need to define the uniaxial stress-strain relationship of concrete in both compression and tension. In the present study, Hognestad (1973) parabola described with the equation below was adopted for the concrete compression behavior. It was assumed that the concrete shows a linear elastic response up to 40 % of the peak stress (Genikomsou et al., 2015; Genikomsou, 2015). In Figure 3.2, the dotted line shows the original curve of the Hognestad parabola, and the gray line shows the Abaqus input. The region enclosed by the gray line has the same area of the region enclosed by the Hognestad parable. Parameters required to determine the parabola are defined based on the material test results of the concrete cores.

$$\sigma_c = f_c' \left[2\left(\frac{\varepsilon}{\varepsilon'_c}\right) - 2\left(\frac{\varepsilon}{\varepsilon'_c}\right)^2 \right], \qquad \text{Equation 3-11}$$

where ε'_c is the strain at the peak stress $f_c^{'}$. The strain at the peak stress ε_c were assumed based on the equation shown below.

$$\varepsilon_c = 1.8 + 0.0075 f_c' \qquad \text{Equation 3-12}$$

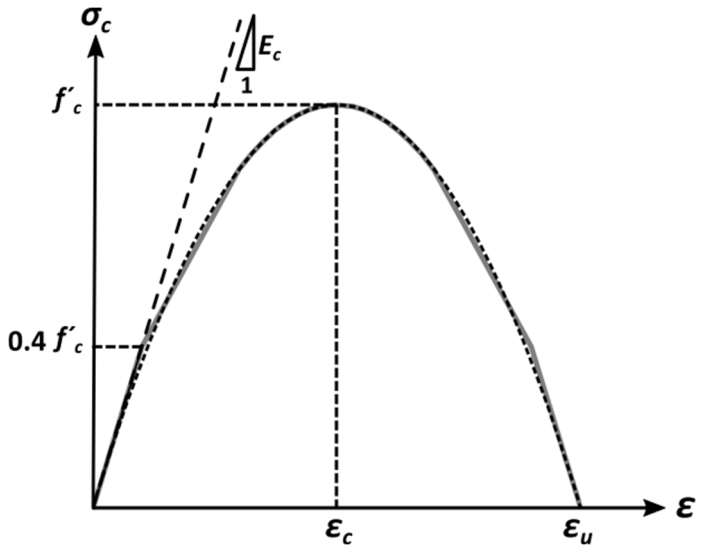

Figure 3.2: Uniaxial stress-strain relationship in compression (reproduced from Genikomso, 2018)

Regarding the tension side of the concrete before the cracking, the linear elastic response was assumed. For the concrete after the cracking, the fracture energy-based cracking criterion proposed by Hillerborg (1976) was used (Dassault Systemes Simulia Corp, 2017). The fracture energy G_f was defined based on CEB-FIP MC 90 with the compressive strength obtained from the concrete cores. The stress-crack displacement relationship was established following Figure 3.3.

$$G_f = G_{f0}\left(\frac{f_{cm}}{10}\right)^{0.7}, \qquad \text{Equation 3-13}$$

where G_{f0} is the base fracture energy which can be calculated from the CEB-FIP MC 90, and f_{cm} is the mean value of the compressive strength of concrete (Comite Euro-International du Beton, 1993). The calculated value of G_f based on CEB-FIP MC 90 in the present study was 0.135 N/mm.

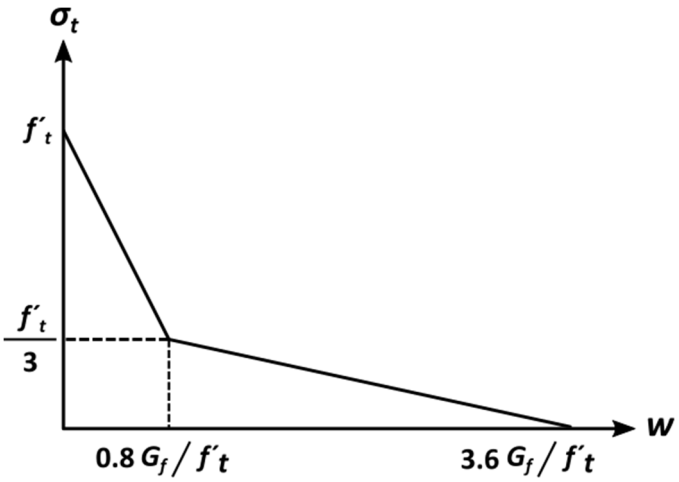

Figure 3.3: Uniaxial stress-crack width relationship (reproduced from Hillerborg, 1985)

The stiffness degradation variable d has great significance when the structures are subjected to cyclic or dynamic loadings (Genikomsou et al., 2015; Huang, 2012). In this study, this variable was omitted because the curved wall specimen was assumed to be subjected to quasi-static loading. Therefore, the analysis model in this study should behave as a plasticity theory-based model (Wahalathantri et al., 2011; Genikomsou, 2015; Wosatko, 2019).

The values of 30-degree and 1.0×10^{-8} were assigned to the dilation angle and viscosity parameter, respectively. These values are based on the parametric studies shown in the later sections. Other parameters for the CDPM were set to the default values provided by Abaqus. The adopted parameters for the CDPM were summarized in Table 3.1.

Table 3.1: Adopted values for parameters of CDPM

Yeild function		Plastic potential function		Viscoplastic regularization
Stress ratio* σ_{b0}/σ_{c0}	Shape factor* K_c	Eccentricity* ϵ	Dilation angle ψ, -degree	Viscosity parameter μ
1.16	0.667	0.1	30	1.0×10^{-8}

* The default value provided by Abaqus R2017x was adopted.

Reinforcing bars and tendons were discretely modeled with truss bar finite elements, which is detailed in the next subsection. In terms of the material model for the reinforcing bars, the classical plasticity model was employed. The engineering stress-strain relationship for the reinforcing bar was adopted based on the trilinear (elastic hardening) model, as shown in Figure 3.4. The adopted mechanical properties for the reinforcing bars were based on the past material test conducted by Choi et al. (2018). The reported yield stress, the tensile strength, and the elastic modulus ware 60.7 ksi (419 MPa), 96.4 ksi (665 MPa), and 28,630 ksi (197,380 MPa), respectively. As for the strands in the tendons, linear-elastic material models were used because the tendon did not yield during the experimental test.

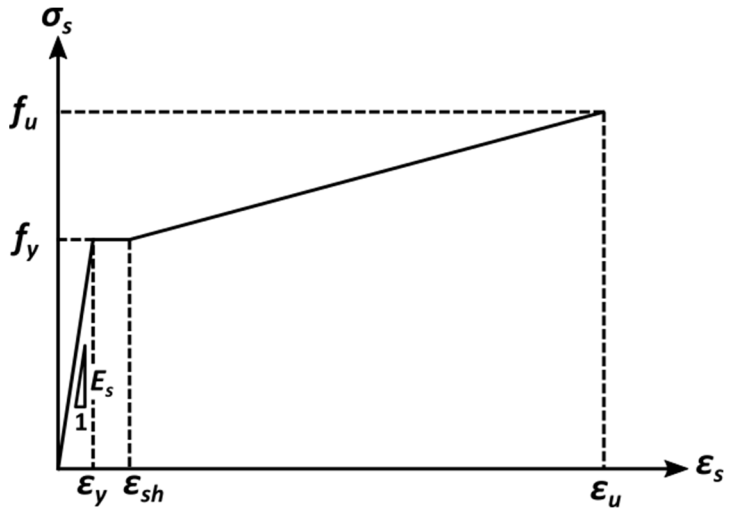

Figure 3.4: Stress-strain relationship for steel (reproduced from Wong et al., 2013)

3.1.2.2 Finite Element Modeling

The geometry of the specimen is considered to be symmetrical in its vertical direction if the friction between the specimen and the floor is negligible, so the upper half of the test specimen was modeled to reduce the computational cost, as shown in Figure 3.5. The analysis model consists of four portions: the curved wall, the dead-end block, reinforcing bars, and a tendon. The curved wall and the dead-end anchor block were modeled with brick elements, which are 20-noded second-order hexahedral elements with the reduced Gaussian integration called C3D20R in Abaqus, which have a 2×2×2 integration scheme (Dassault Systemes Simulia Corp, 2017). This element was selected to avoid the shear locking and the spurious zero-energy numerical effect. The dead-end block was heavily reinforced, and no damage was observed, so its stiffness was set to be significantly large relative to the other portions.

The horizontal and vertical reinforcing bars were modeled with truss elements and constrained to the brick elements using the embedded technique provided by Abaqus. With

this method, the reinforcing bars behave as if those are perfectly bonded to the surrounding concrete. The tendon was also modeled with truss elements, which will be detailed later.

The vertical movement was only restrained in order to model a symmetric boundary condition at the bottom of the model. The live-end block was not modeled explicitly; instead, fixed boundary conditions were applied at the interface where the curved wall adjoins the live-end anchor block. A displacement was enforced at one end of the truss elements representing the tendon to apply the prestressing load to the model.

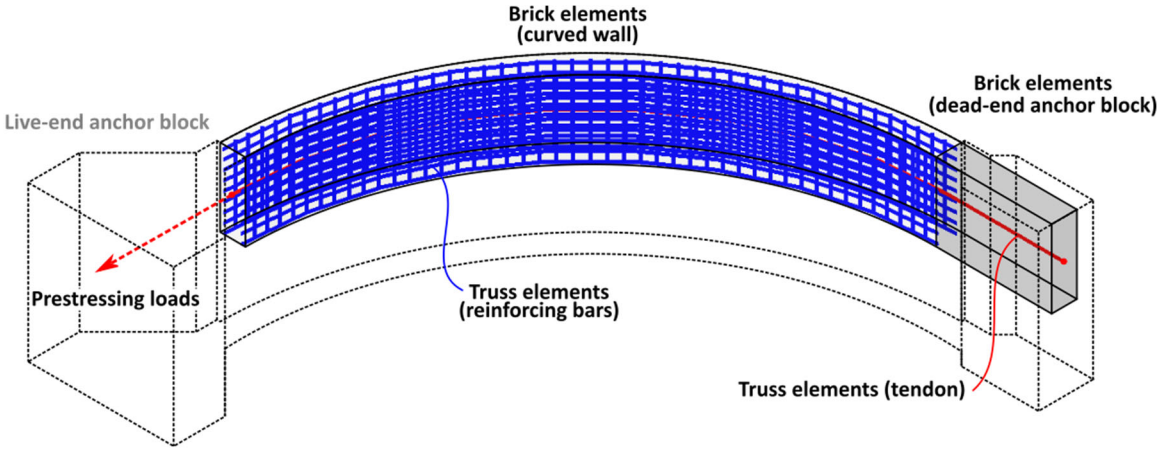

Figure 3.5: Abaqus analysis model

The unbonded tendon was modeled using the spring system method introduced by Huang (2012). Instead of modeling holes, ducts, and strands explicitly with brick elements, this method adopts a combination of truss and spring elements for modeling the behavior of strands within a duct so that the computational cost can be significantly reduced. The post-tensioning tendon system model consists of three parts: strands (truss elements), a virtual tendon (truss elements), and springs. The truss elements for the strands and the virtual tendon shared the same geometry. They were placed at the centerline of the wall section in the model since the tendon was placed considering the eccentricity of the strands

in the actual test (see Figure 2.1). The virtual tendon is constrained by the concrete using the embedded technique of Abaqus and connected to the strands with spring elements. The node for the strands at the dead-end was directly related to the brick element to represent the anchorage of the strands. The stiffness of the virtual tendon was set to a minimal such that the influence of virtual tendon on the concrete behavior is negligible. As a result, the prestressing load transfer mechanism in concrete can be effectively simulated in the analysis model. (Huang, 2012).

The spring system method proposed by Huang (2012) used SPRINGA element, which has length and can be used in both the implicit and explicit solver of Abaqus, to relate the strands and the virtual tendon. However, in the present study, SPRING2 elements with zero-length were employed. This element can show similar behavior to the link elements implemented in VecTor4, representing the interaction between the strands and the tendon, which will be detailed in the later section. Each set of two nodes at the same location in the tendon was connected with zero-length springs in three directions: a normal direction to the tendon, a tangential direction along the tendon, and a vertical direction (see Figure 3.6). The springs in the normal and the vertical directions were defined with sufficiently large stiffness to constraint the strands and the virtual tendon in those two directions. An appropriate stiffness was assigned to the springs in the tangential direction to account for the friction losses of prestressing strands. Friction losses are typically induced by the wobble and curvature of a tendon profile.

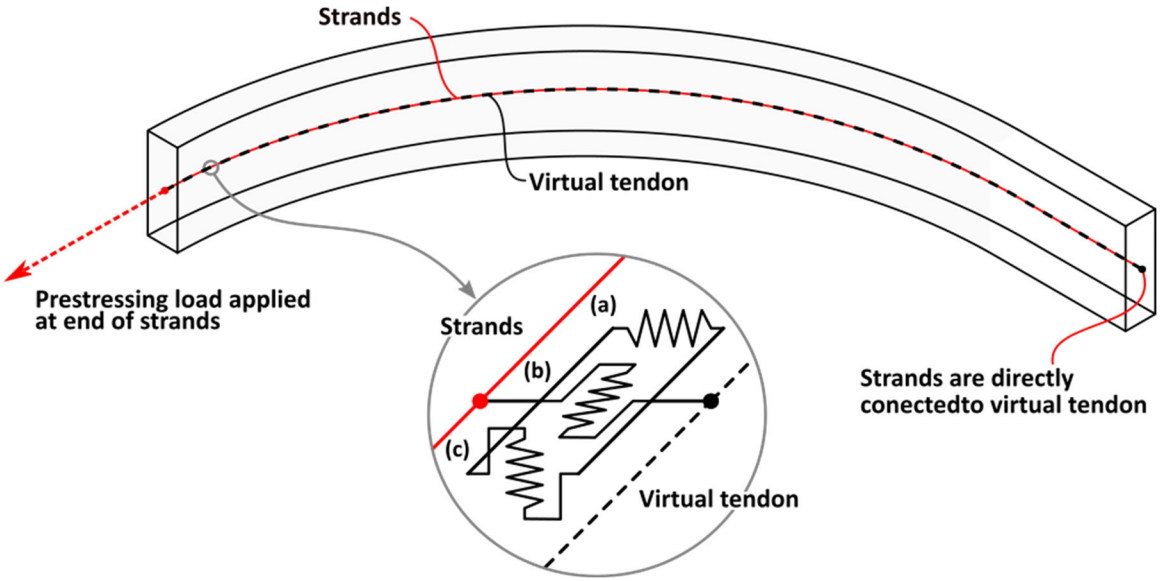

Figure 3.6: Schematics of zero-length springs defined between strands and tendon: (a) normal direction; (b) tangential direction; and (c) vertical direction

Regarding the curved wall test specimen, the curvature of the tendon profile is considered as the primary source of friction losses (Choi, 2018). Therefore, in this study, friction losses were set only in the curved portion. The stiffness of springs representing the friction losses was adjusted based on the test results and checking the relationship between the prestressing loads at the live-end and the dead-end in each nonlinear analysis (see Figure 3.7).

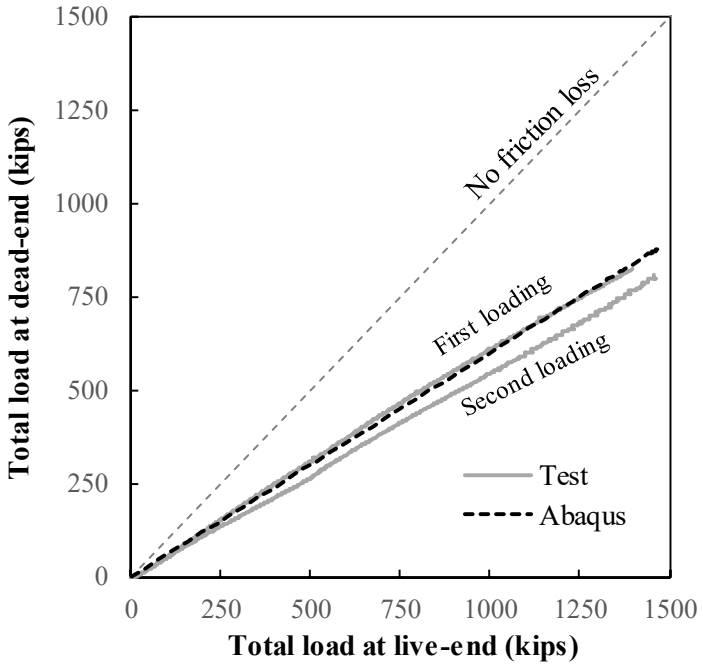

Figure 3.7: Example of adjusting spring stiffness (prestressing load at the live-end vs. at the dead-end)

3.1.4. Validation: Parameter Investigation

This section will present the parameter sensitivity studies regarding mesh density, dilation angle, and viscosity parameters to discuss the validity of the model for Abaqus.

3.1.4.1 Mesh Density

The mesh sensitivity study was conducted to investigate the mesh convergence and the computational cost. The sample problem of the linear elastic analysis for the cantilever beam subjected to end shear load provided by the Abaqus manual suggests that the C3D20R brick elements can give sufficiently accurate solutions even if the model has only one element through the thickness (Dassault Systemes Simulia Corp, 2017). However, the problem of interest in this thesis is expected to show severe nonlinearity. Besides, the model is better to be divided into even numbers in its through-thickness direction to place

the tendon elements along the mesh line of the brick elements. Based on the above discussion, the minimum number of the elements through the thickness was set to four. Consequently, the models with element sizes of 1.0 in. (12 elements through the thickness), 1.5 in. (8 elements through the thickness), 2.0 in. (6 elements through the thickness) and 3.0 in. (4 elements through the thickness) were generated, respectively (see Figure 3.8).

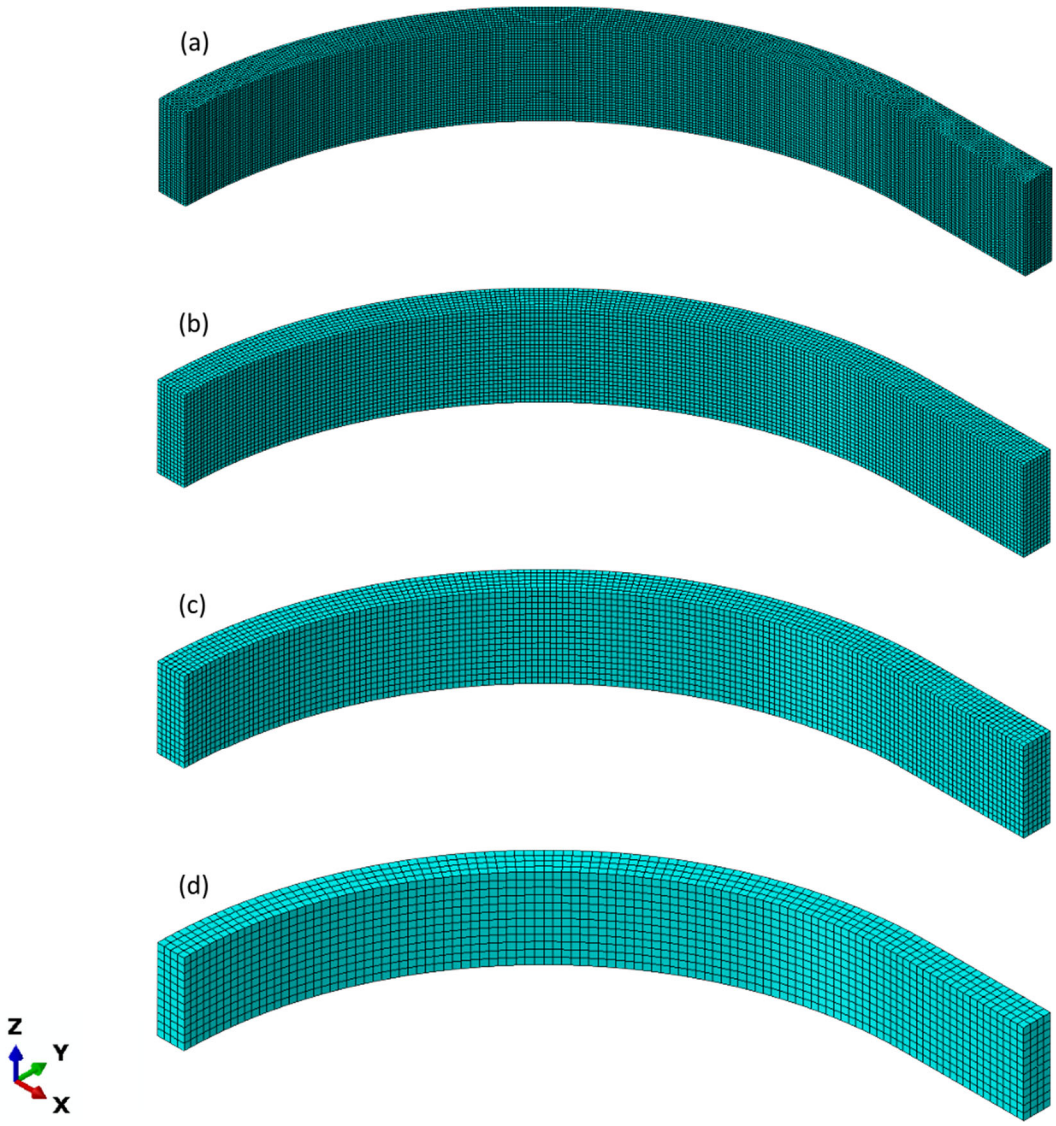

Figure 3.8: Generated model with element size of; (a) 1.0 in. (25.4 mm), (b) 1.5 in. (38.1mm), (c) 2.0 in. (50.8 mm), and (d) 3.0 in. (76.2 mm)

The estimated ultimate loads are summarized in Table 3.2. The model with the element size of 1.0 in. to 2.0 in. estimated the ultimate load with the error within 1.1% compared to the actual test result. The analysis with the element size of 3.0 in. overestimated the ultimate load by 5.2%. Given the variability in the material properties, it can be said that the estimated ultimate loads showed good agreement with the actual test result.

Table 3.2: Estimated ultimate loads depending on the element size

Element size mm (in.)	Estimated ultimate load kips (kN)	Error* (%)
1.0 (25.4)	1450 (6448)	-0.7
1.5 (38.1)	1445 (6427)	-1.1
2.0 (50.8)	1466 (6521)	0.4
3.0 (76.2)	1536 (6831)	5.2

* The ultimate load of the test was 1460 kips (6496 kN)

Figure 3.9 depicts the relationship between the applied prestressing load and the through-thickness expansions at the height of the upper tendon. In the early stage, the models are governed by the linear-elastic regime of the concrete material. After the prestressing load surpassing approximately 1000 kips, the responses from the analysis models vary depending on the mesh density. It is clearly shown that the models with coarse meshes tend to show stiffer responses in the inelastic region.

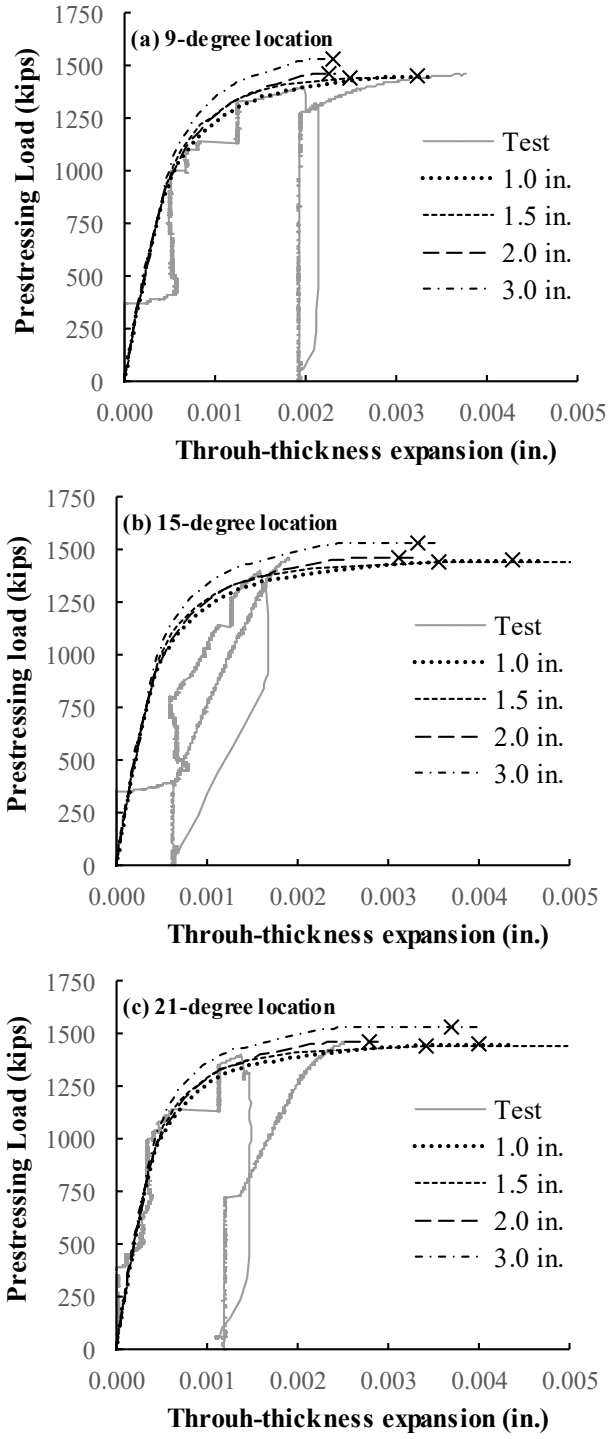

Figure 3.9: Through-thickness expansion (mesh sensitivity study) at location of; (a) 9-degree, (b) 15-degree, and (c) 21-degree

The cracked concrete elements should have the integration points with the tensile equivalent plastic strain $\tilde{\varepsilon}_t^{pl}$ greater than zero. Thus, the distribution of the tensile equivalent plastic strain $\tilde{\varepsilon}_t^{pl}$ can visualize the crack pattern of a model with the CDPM (Genikomsou, 2015; Dassault Systemes Simulia Corp, 2017). Figures 3.10, 3.11, and 3.12 show the distribution of tensile equivalent plastic strain at the estimated ultimate load. From Figure 3.10, a horizontal crack along with the duct location, which is deemed a flexural crack, can be found in the inner surface of the analysis models. This crack pattern is also observed from the actual test specimen during the visual inspection. In Figure 3.11, it is found that the delamination crack occurred at approximately 15- to 21-degree locations in the analyses. On the other hand, the actual critical section in the test seems to be at around 9-degree based on the observation of the through-thickness expansions (Choi 2020). The estimated through-thickness expansions at the 9-degree location tend to be smaller than the actual test results in all cases (see Figure 3.9). It was deemed that the fixed condition applied at the end of the live-end anchor block side excessively confined the curved wall section. Figure 3.12 depicts the sectional view of the distribution of equivalent plastic strains. The analysis models except for the model with the element size of 76.2mm implies that the test specimen experienced the local shear cracking, which agrees with the inspection of the actual test after the delamination failure.

Based on this study, it can be concluded that the model with finer mesh may give solutions with better quality. However, the concrete is assumed to be homogeneous material in the CDPM. It is better to have spacings of integration points larger than the maximum aggregate size (1.0 in. (25.4mm) for the present specimen) to avoid violating this assumption. Therefore, the element size of larger than 2.0 in. (50.8 mm) can be preferable for 20-noded brick elements with reduced integration, which have a 2×2×2 integration scheme.

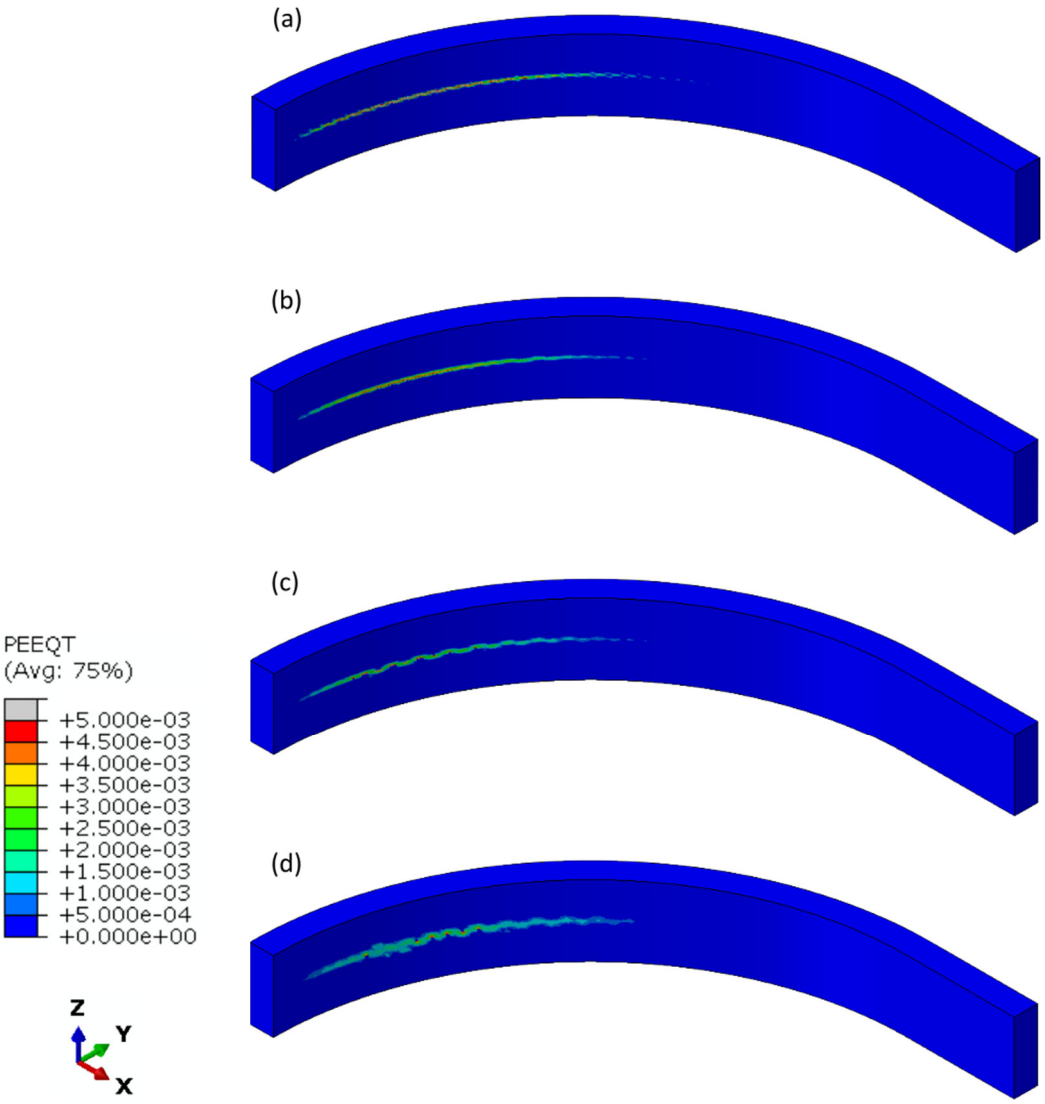

Figure 3.10: Overview of crack pattern with element size of; (a) 1.0 in., (b) 1.5 in., (c) 2.0 in., and (d) 3.0 in.

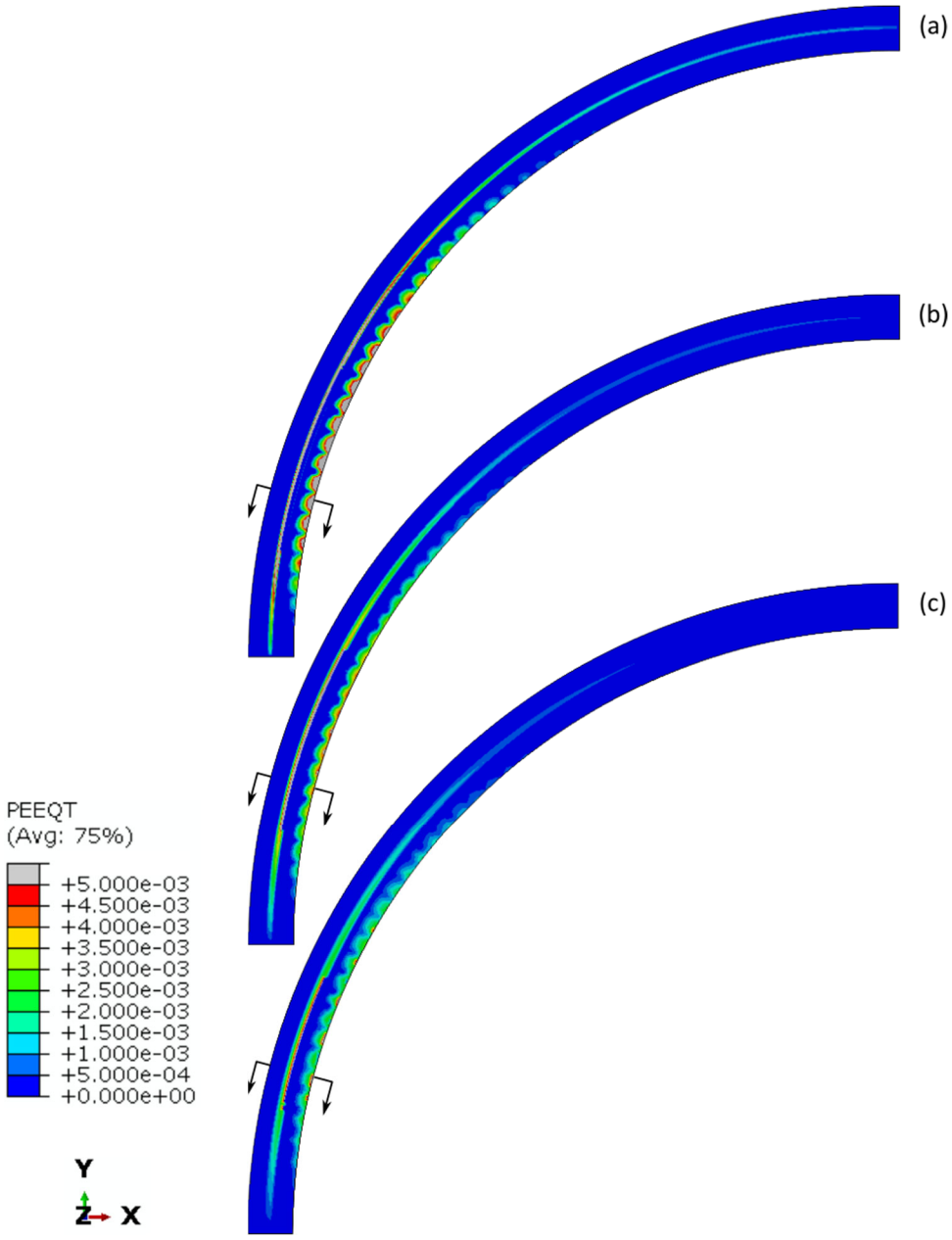

Note: the sectional views indicated in the figures are shown in Figure 3.12.

Figure 3.11: Horizontal sectional view at duct location and crack patterns observed from the models with element sizes of; (a) 1.0 in., (b) 1.5 in., (c) 2.0 in., and (d) 3.0 in.

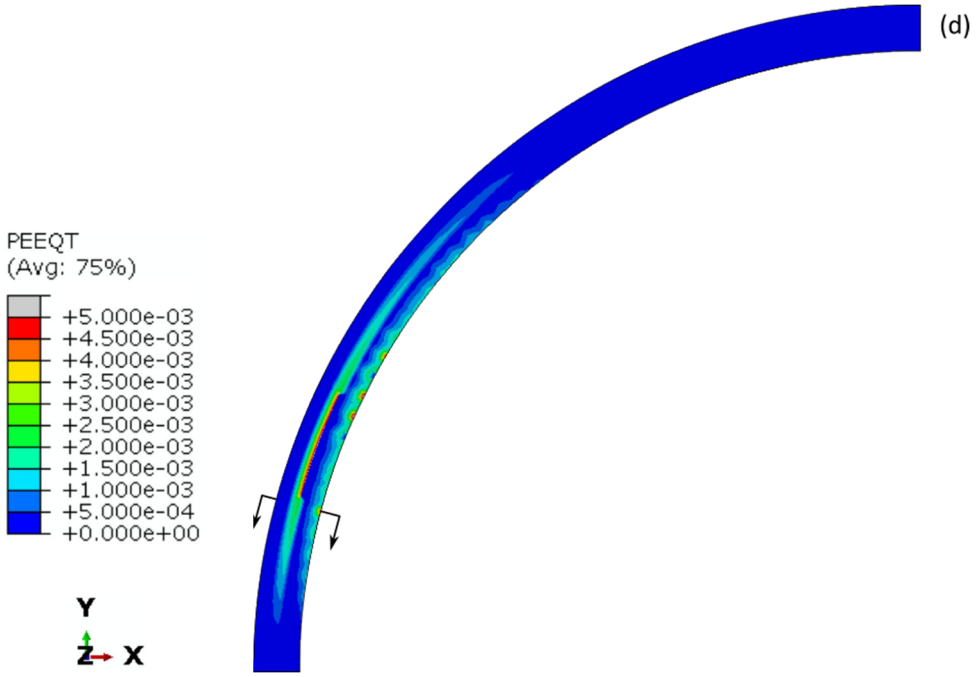

Note: the sectional views indicated in the figures are shown in Figure 3.12.

Figure 3.11 (cont.): Horizontal sectional view of crack pattern at height of upper tendon with element size of; (a) 1.0 in., (b) 1.5 in., (c) 2.0 in., and (d) 3.0 in.

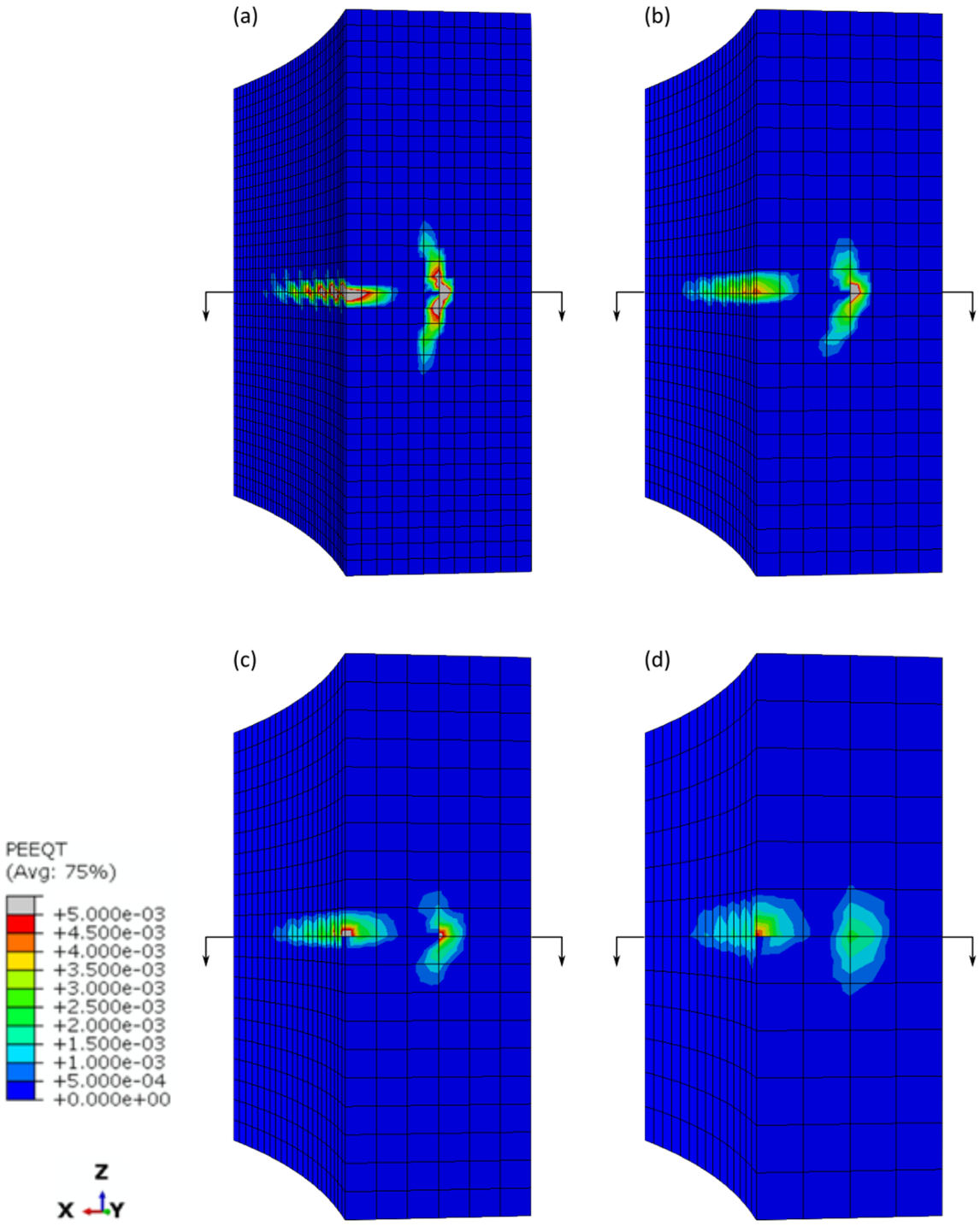

Note: the horizontal sectional views indicated in the figures are shown in Figure 3.11.

Figure 3.12: Sectional view of crack pattern at 15-degree location with element size of; (a) 1.0 in., (b) 1.5 in., (c) 2.0 in., and (d) 3.0 in.

3.1.4.2 Dilation Angle

Dilation angle for the CDPM may considerably influence the analysis results. Lee and Fenves (1998) set the value of 0.2 for the parameter for dilatancy. This value corresponds to the dilation angle of 36-degree in the CDPM of Abaqus (Wosatko, 2019). Genikomsou (2015) explored the values between 20 to 42-degree for the dilation angle and concluded that the appropriate dilation angle could be 42-degree for the reinforced concrete slabs subjected to the punching shear. Based on these past studies, three different dilation angles (20-degree, 30-degree, and 40-degree) were selected to investigate the influence of dilation angles on the accuracy of analysis results. The adopted element size of the model for this study was 2.0 in. (50.8 mm).

The estimated ultimate loads obtained from the analyses are summarized in Table 3.3. The earned ultimate load with the dilation angle of 30-degree shows the minimum error among the analysis cases conducted for this study.

Table 3.3: Estimated ultimate loads depending on dilation angle

Dilation angle (degree)	Estimated ultimate load kips (kN)	Error* (%)
20	1381 (6143)	-5.4
30	1466 (6521)	0.4
40	1635 (7272)	12.0

* The ultimate load of the test was 1460 kips (6496 kN)

The through-thickness expansions obtained from each analysis are shown in Figure 3.13. From Figure 3.13, it can be observed that the larger dilation angle tends to overestimate both capacity and through-thickness expansions than the actual measured values. Overall, the analysis with the dilation angle of 30-degree shows the best agreement with experimental results among the examined dilation angles.

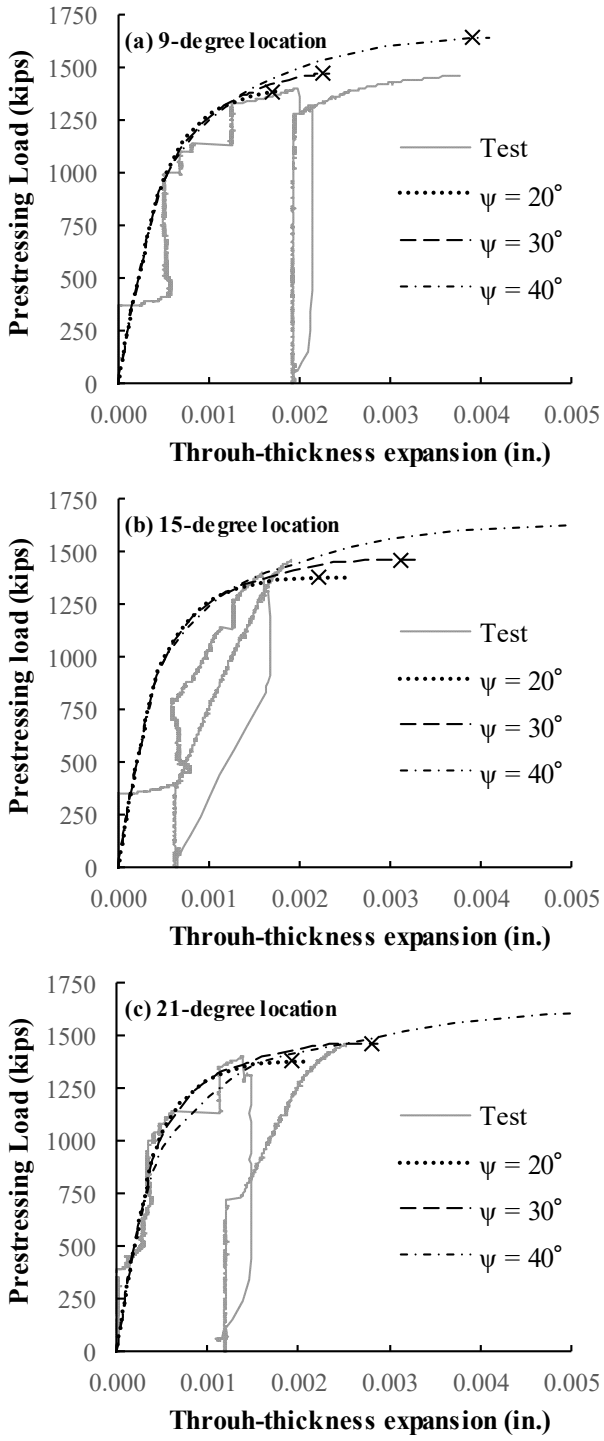

Figure 3.13: Through-thickness expansion at location of; (a) 9-degree, (b) 15-degree, and (c) 21-degree

The tensile equivalent plastic strain distribution representing the crack pattern of the analysis results is depicted in Figure 3.14 to Figure 3.16. From Figure 3.14, the longer horizontal crack induced by the sectional bending moment can be observed in the models with the lager dilation angle. Figure 3.15 shows that the horizontal crack due to the sectional flexure spreads over a wider area when a lager dilation angle is adopted. Figure 3.16 depicts sectional flexural and shear crack patterns at the 15-degree location. It can be concluded that the analysis with a lager dilation angle results in a sectional flexure-dominant response, i.e., horizontal crack dominant. In contrast, the sectional shear-dominant response is observed for the model with a smaller dilation angle. Based on the observation of the analysis results, the dilation angle of 30-degree was selected and used for one of the main input variables in analyses.

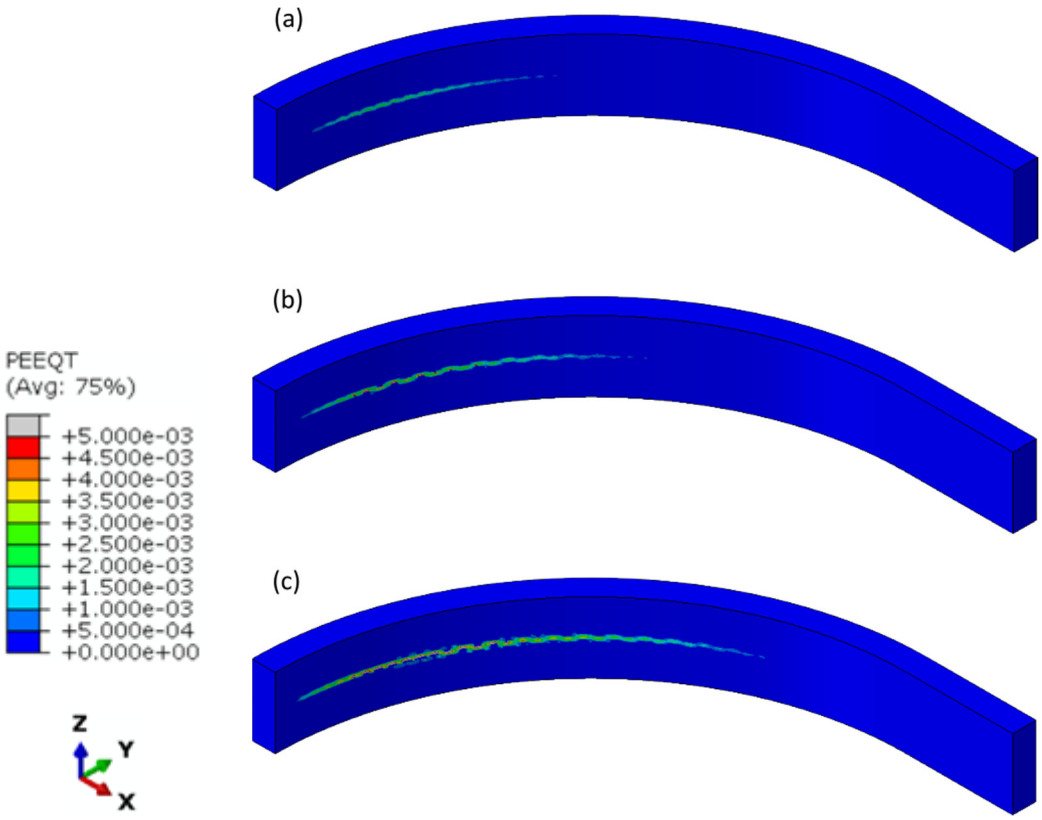

Figure 3.14: Overview of crack pattern (equivalent tensile plastic strain distribution) with dilation angle of; (a) 20-degree, (b) 30-degree, and (c) 40-degree

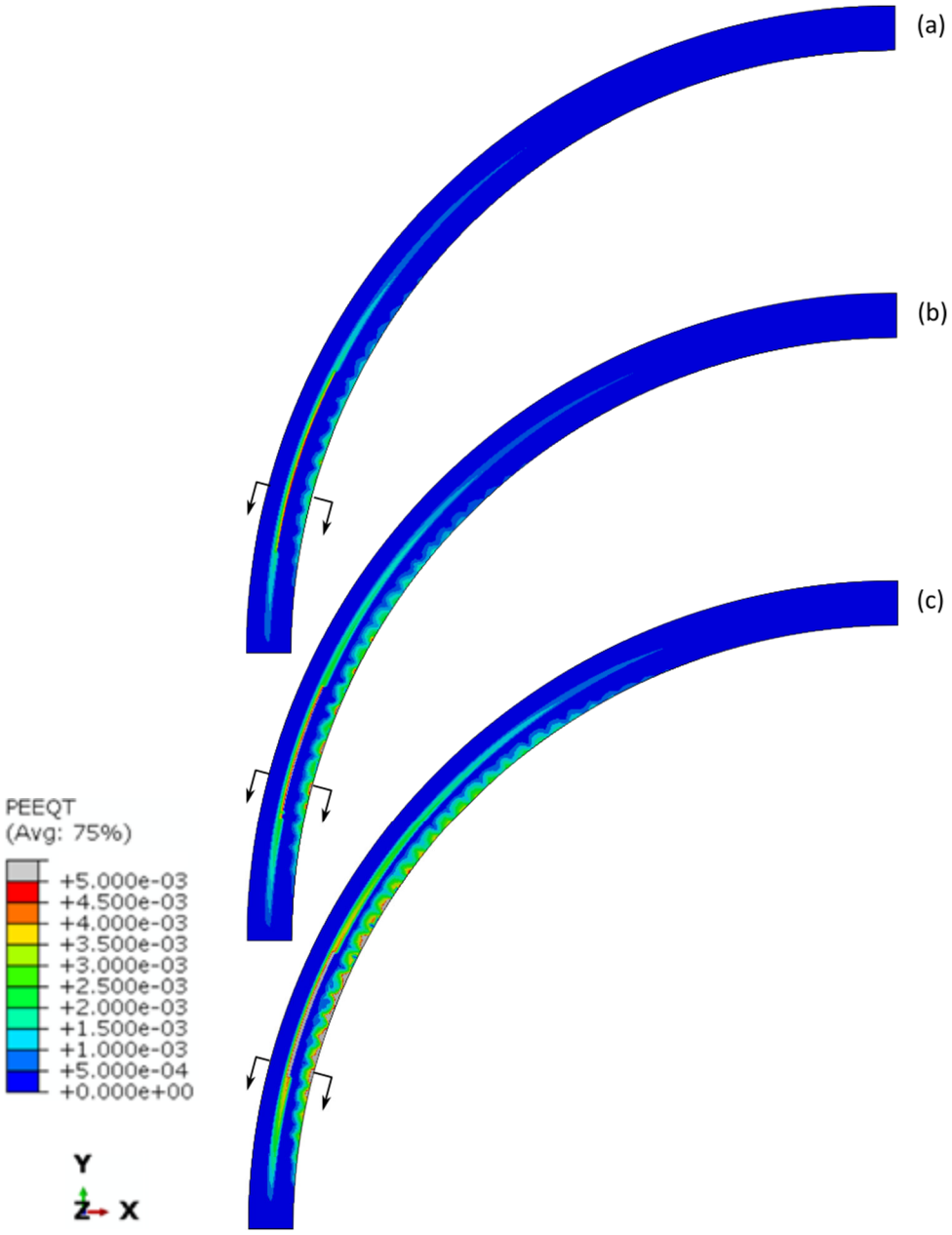

Note: the sectional views indicated in the figures are shown in Figure 3.16.

Figure 3.15: Horizontal sectional view of crack pattern at height of upper tendon with dilation angle of; (a) 20-degree, (b) 30-degree, and (c) 40-degree

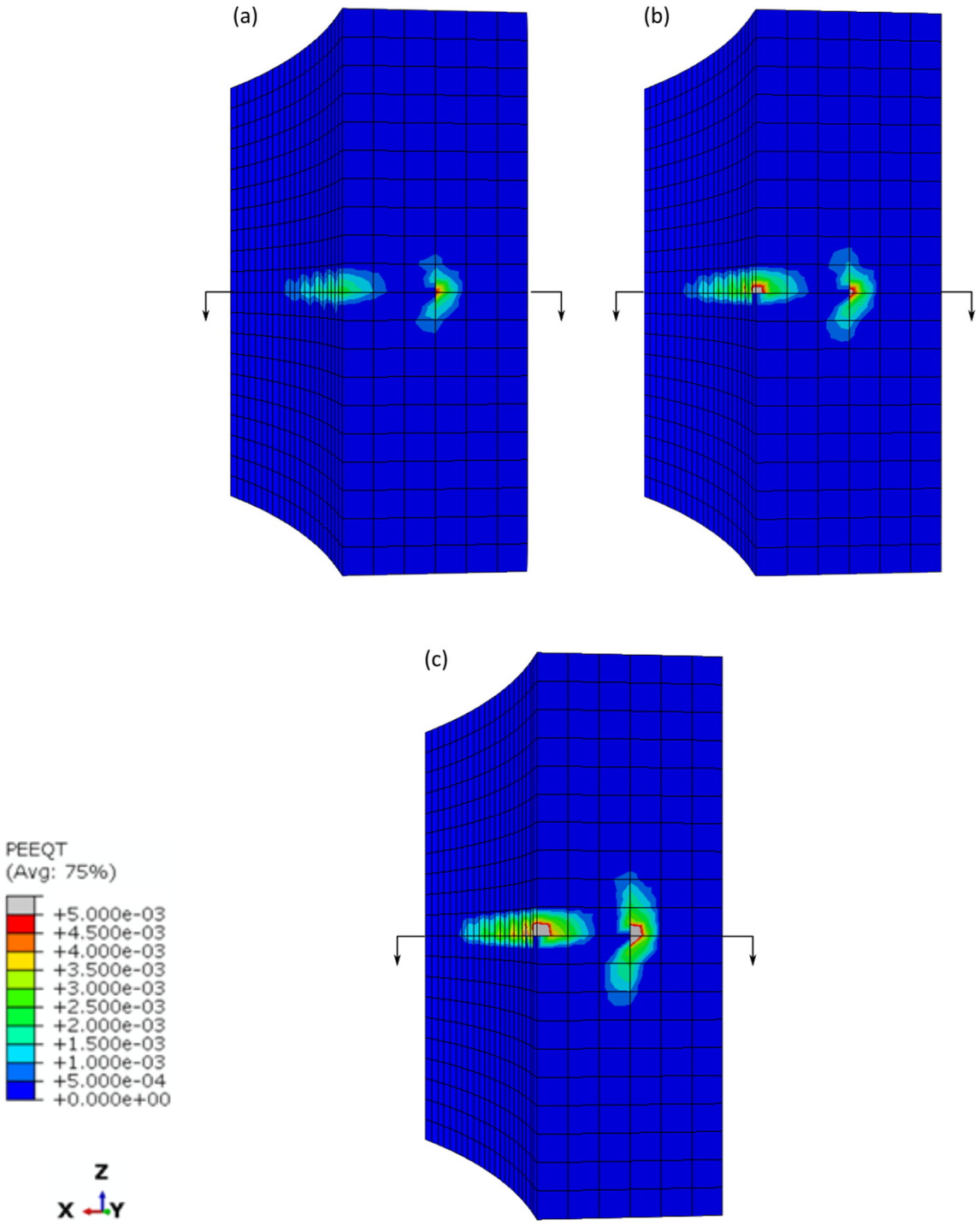

Note: the horizontal sectional views indicated in the figures are shown in Figur 3.15.

Figure 3.16: Sectional view of crack pattern at 15-degree; (a) 20-degree, (b) 30-degree, and (c) 40-degree

3.1.4.3 Viscosity parameter

The viscosity parameter μ can help the convergence of the analysis with softening materials. Still, it should be sufficiently small relative to the time increment of the analysis as the impact of the viscosity parameter depends on the time increment of analyses (Dassault Systemes Simulia Corp, 2017). On the other hand, Abaqus automatically controls the time increment of analyses. Ideally, the analysis without using this parameter can give the most appropriate solutions. However, many problems involve severe material nonlinearity, and such problems are rarely solved without the viscosity parameter. Therefore, the additional analysis with the viscosity parameter of 0.0 was conducted to check the suitability of the chosen value (μ=1×10^{-8}). The model with the element size of 2.0 in. (50.8 mm) was used for this study.

The through-thickness expansions obtained from the analyses are compared in Figure 3.17. The overall trends of those two analysis results were almost the same. Figure 3.18 shows the close-up view of the area around the ultimate load in Figure 3.17 (b). It can be observed that the analysis with the viscosity parameter of 0.0 does not show the drop of the prestressing load. This is because the analysis with the viscosity parameter of 0.0 stops before the prestressing load starts to drop due to the convergence difficulty.

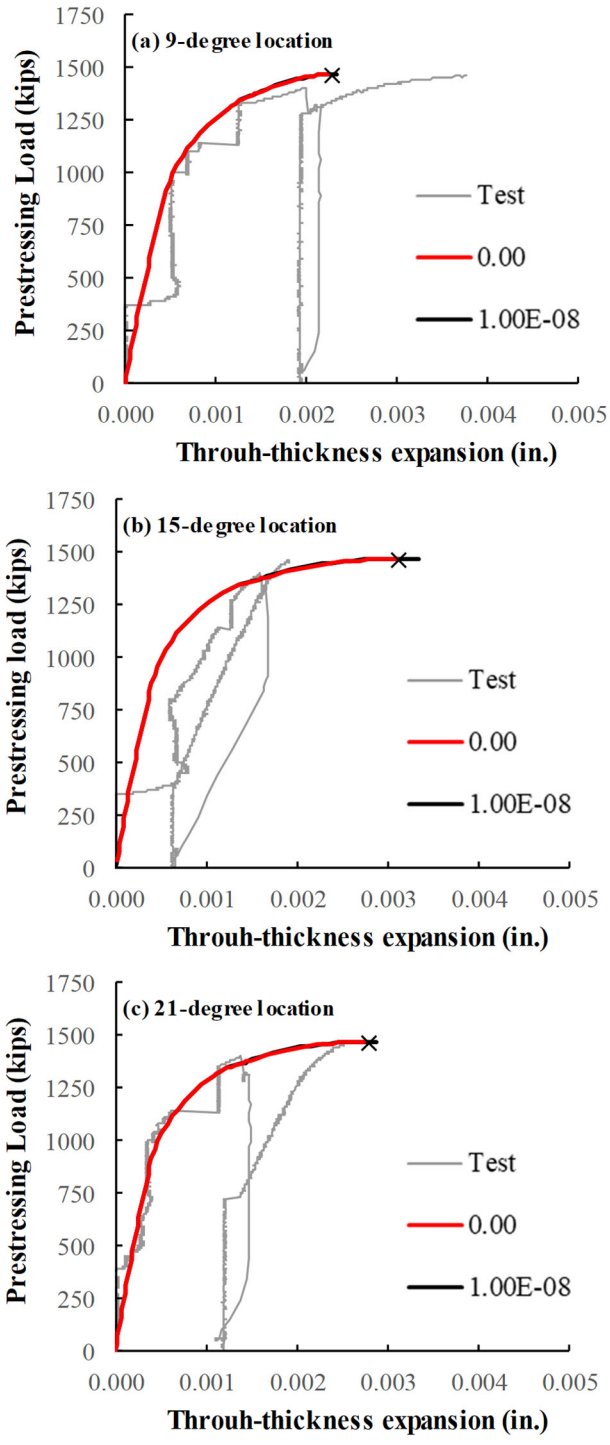

Figure 3.17: Analytically obtained and experimentally measured through-thickness expansions at locations of ; (a) 9-degree, (b) 15-degree, and (c) 21-degree

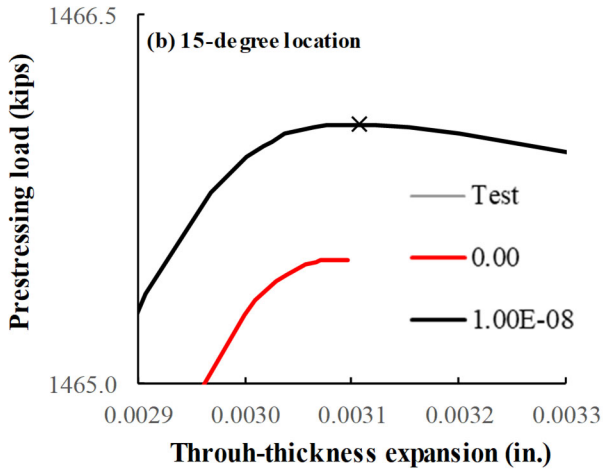

Figure 3.18**:** Close-up view of Figure 3.17 (b)

The tensile equivalent plastic strain distribution representing the crack pattern is depicted in Figure 3.19 to Figure 3.21. Figure 3.19, 3.20, and 3.21 show the overview, the horizontal sectional view at the height of the tendon, and the sectional view at the 15-degree location of the model, respectively. The shown figures with the viscosity parameter of 0.0 were taken at the last step of the analysis, whereas the figures with viscosity parameter of 1×10^{-8} were at its ultimate load. It should be noted that the deformation levels where those figures were taken are almost the same, as can be seen in Figure 3.18. The analyses show almost the same equivalent tensile plastic strain pattern. It can be concluded that the value of 1×10^{-8} can enable the analysis to show the peak of the prestressing load without a huge impact on the analysis results.

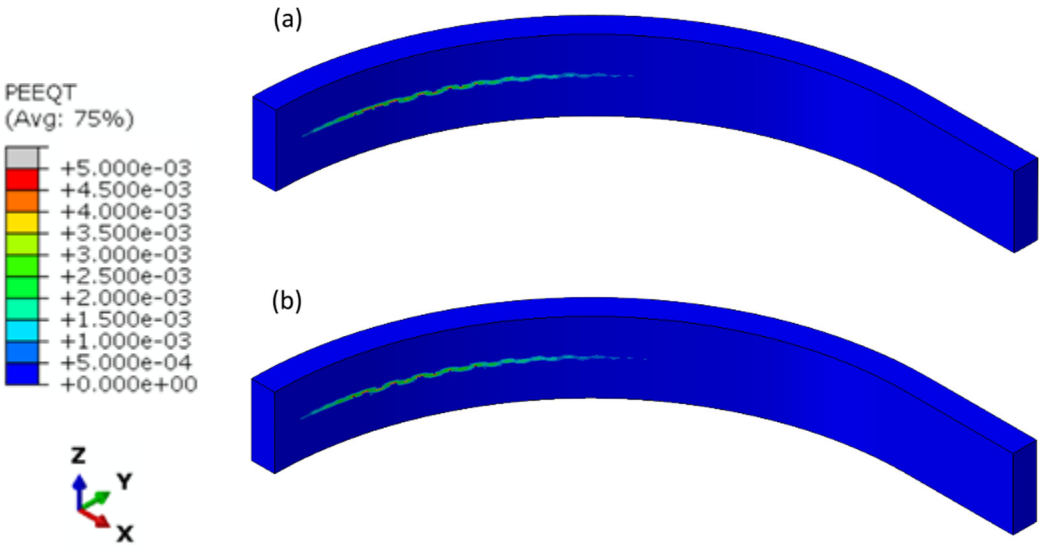

Figure 3.19: Overview of crack pattern viscosity parameter of; (a) 0.0, and (b) 1×10^{-8}

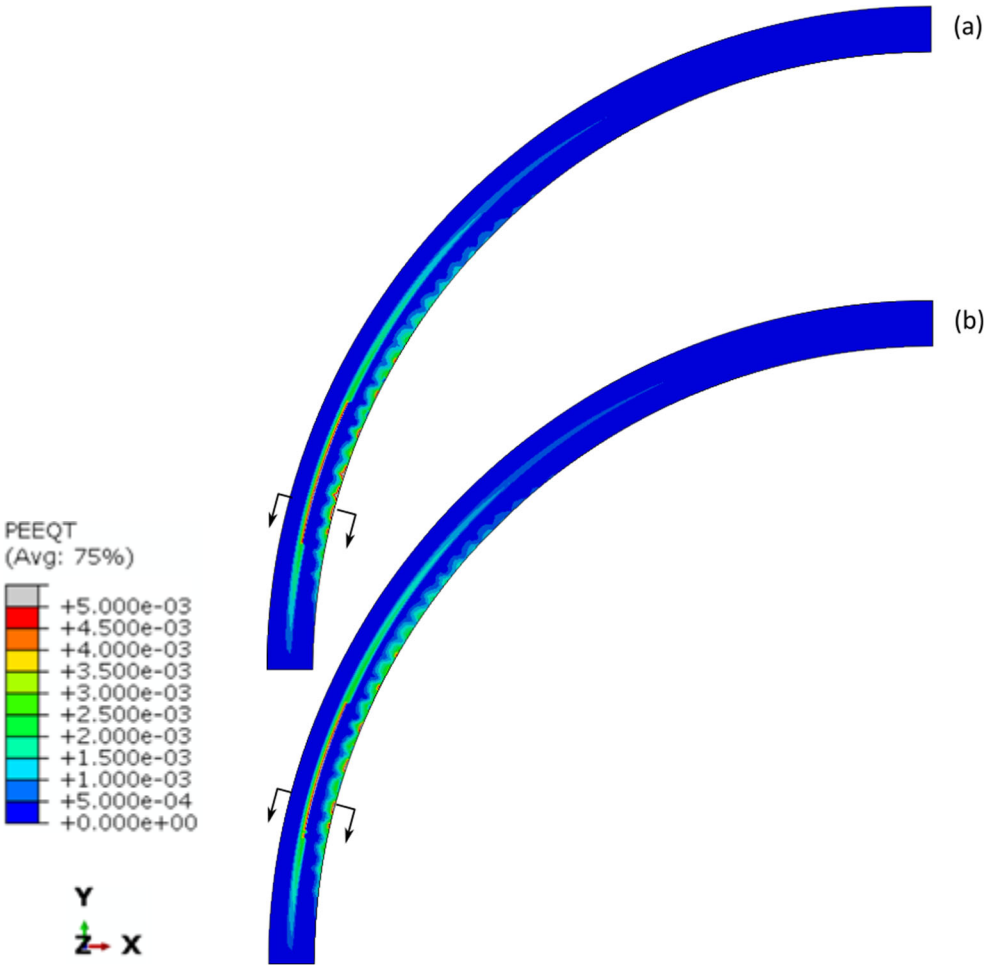

Note: the sectional views indicated in the above figures are shown in Figure 3.21.

Figure 3.20: Horizontal sectional view of crack pattern at height of upper tendon (tensile equivalent plastic strain) with viscosity parameter of; (a) 0.0, and (b) 1×10^{-8}

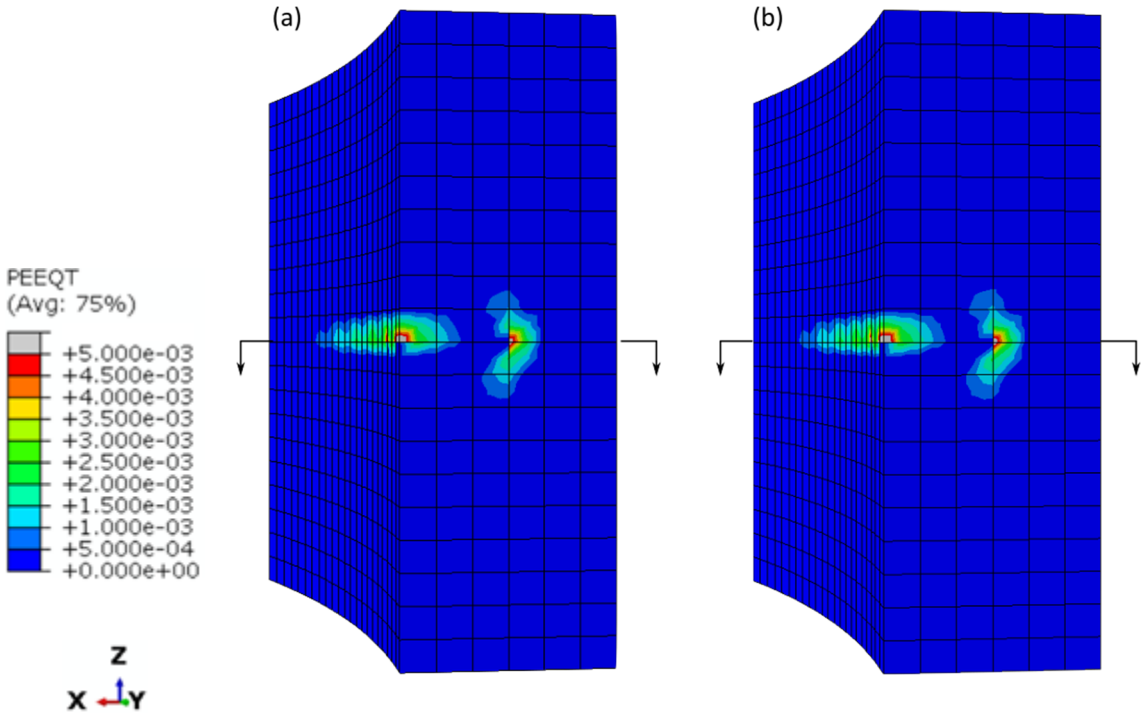

Note: the horizontal sectional views indicated in the figures are shown in Figure 3.20.

Figure 3.21: Sectional view of crack pattern at 15-degree location with viscosity parameter of; (a) 0.0, and (b) 1×10^{-8}

3.2. VECTOR4

The academic program VecTor4 belongs to the suite of VecTor programs. VecTor is a nonlinear finite element program for the concrete structures developed at the University of Toronto. Among the series of the VecTor programs, VecTor4 is specialized in the shell and slab structures. The version of the VecTor4 program adopted in the present study is a modified version reported by Choi (2018), which was redeveloped by Hrynyk (2013).

3.2.1. Disturbed Stress Field Model (DSFM)

The theoretical basis governing the behavior of reinforced concrete in VecTor4 is the Disturbed Stress Field Model (DSFM) proposed by Vecchio (2000), which was developed as an extension of the Modified Compression Theory (MCFT). The DSFM treats cracked reinforced concrete as an orthotropic nonlinear elastic material based on a smeared hybrid rotating-fixed crack model (Vecchio, 2000).

In the MCFT, cracked reinforced concrete was assumed to be a fully rotating smeared crack model (Vecchio and Collins, 1986). Cracked reinforced concrete elements were governed by equilibrium, compatibility, and constitutive relations of cracked concrete and reinforcing bars, which were formulated in an averaged sense. Though the MCFT was described in an averaged sense, local stress conditions were checked at crack locations. The constitutive relations derived based on the series of reinforced concrete panel tests at the University of Toronto. The reduction of strength and stiffness of cracked concrete in compression due to the high tensile strains in the direction normal to the compression was considered. Also, the MCFT included a tension stiffening effect in the concrete between cracks.

In comparison to the MCFT, the primary advancement in the DSFM was the consideration of shear slip phenomena on crack surfaces in compatibility conditions. The

inclusion of crack slips allows the divergence of principal stress and principal strain directions of elements, which is more consistent with the results of the panel tests (Vecchio, 2000; Vecchio, 2001).

It should also be mentioned that the VecTor programs use the secant stiffness algorithm. With the secant stiffness algorithm, the asymmetry in the stiffness matrix is avoided in the numerical implementation (Vecchio, 2001; Selby and Vecchio, 1997).

3.2.2. Shell Element with Layered Approach

In VecTor4, the heterosis type shell element is adopted to maintain the efficiency of the computational cost of the shell elements while avoiding shear locking and the spurious zero-energy effect. The heterosis shell element takes advantage of both serendipity shape functions and Lagrange shape functions. Each nine-noded shell element has 13 Gaussian integration points, of which 9 points are used for bending and 4 points for shear (Hrynyk and Vecchio, 2015; Hrynyk, 2013).

The layered approach is employed to consider the nonlinear distribution of in-plane stresses and stiffnesses through the thickness of the shell (see Figure 3.22). In the layered approach, the local stresses are assumed to be constant over the height of each layer. In-plane reinforcement are also defined as discrete layers in shell elements with a smeared manner. In an effort to consider the out-of-plane shear, a parabolic shear strain distribution is assumed, which results in better accuracy of the out-of-plane behavior of the shell elements. The sectional forces are obtained by integrating the stresses within a shell element consists of concrete and steel layers (Hrynyk and Vecchio, 2015).

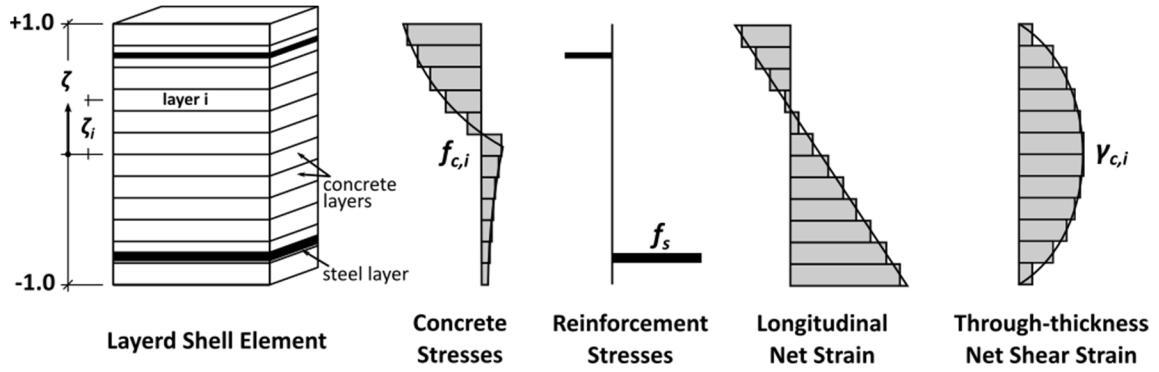

Figure 3.22: Shell element with layered approach (adapted from Hrynyk and Vecchio 2017)

In general, the out-of-plane normal stress is assumed to be negligible in shell elements. The original formulation in the redeveloped version of VecTor4 by Hrynyk (2013) enforces the zero out-of-plane normal stress distribution over the height of shell elements. However, the prestressing tendons with curved profiles induce out-of-plane normal stresses, and these stresses may result in concrete delamination. Thus, Choi (2018) modified the out-of-plane normal stresses in each layer to account for the variation of the out-of-plane normal stresses due to the post-tensioning of the curved walls, yet the equilibrium conditions of shells still hold. In the modified version of VecTor4, the non-zero normal stress distribution with a centrally-located (mid-depth) tendon shown in Figure 3.23, which is the function of the location of the truss element representing the tendon duct, is enforced through the depth of the shell elements (Choi, 2018). The delamination cracking is captured using the Mohr-Coulomb criterion. Once the out-of-plane normal stress satisfies the criterion, the out-of-plane stiffnesses of outer layers within a shell element are automatically reduced. Additionally, the out-of-plane stresses normal due to prestressing force are expected to concentrate in the vicinity of the duct and rapidly decay as the in-plane distance from the tendon increases. A simplified exponential function representing the decaying of the out-of-plane normal stresses due to the stress concentration (Acharya

and Menon 2003) was also incorporated into the modified version of VecTor4 as a decaying factor K_d to account for the in-plane variation of the out-of-plane normal stresses (see Figure 3.24).

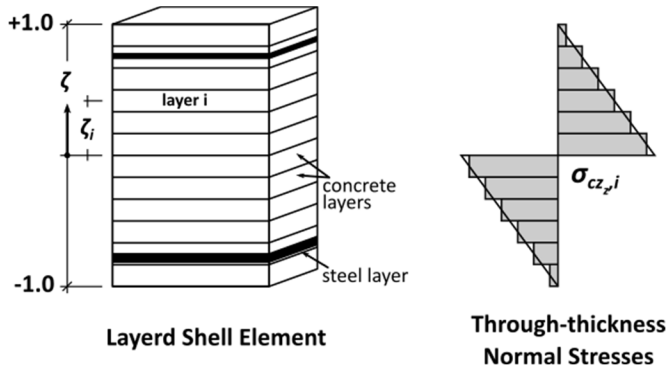

Figure 3.23: Normal stress distribution for centrally located (mid-depth) tendon (adapted from Choi, 2018)

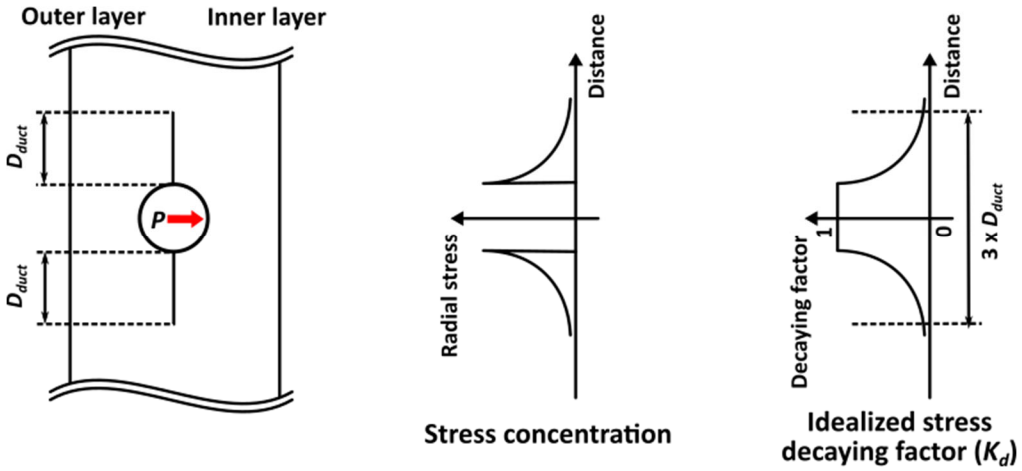

Figure 3.24: Stress decaying factor (adapted from Choi, 2018)

3.2.3. Modeling of Curved Wall Specimen

3.2.3.1. Behavioral Model Options and Parameters for Material models

VecTor4 offers multiple options for the material and behavioral models. The default material and behavioral models provided by VecTor4 are summarized in Table 3.4. It should be noted that the subroutine for the delamination failure was incorporated into the modified version of VecTor4 by Choi (2018) but not listed in Table 3.4.

Table 3.4: Behavioral models (adapted from Hrynyk, 2013)

Concrete Models	
Compression Base Curve	: Hognestad (parabola)
Compression Post-Peak	: Modified Park-Kent
Compression Softening	: Vecchio 1992-A
Tension Stiffening	: Modified Bentz
Tension Softening	: Linear
FRC Post-Crack Tension	: SDEM
Confined Strength	: Kupfer / Richart
Dilatation	: Variable - Kupfer
Cracking Criterion	: Mohr-Coulomb (stress)
Crack Stress Calculation	: Basic (DSFM/MCFT)
Crack Width Check	: Crack Limit (agg/2.5)
Crack Slip Calculation	: Walraven
Hysteretic Response	: Nonlinear w/ Plastic Offsets

Reinforcement Models	
Hysteretic Response	: Bauschinger (Seckin)
Compression Post-Peak	: Tassios (crack slip)

Analysis Options	
Shear Analysis Mode	: Parabolic Shear Strain
Strain History	: Considered
Strain Rate Effects	: CEB/Malvar-Crawford
Structural Damping	: Rayleigh
Geometric Nonlinearity	: Considered
Crack Allocation	: Uniform

The material test results shown in Table 2.1 were directly used as mechanical properties for concrete and steel required in VecTor4.

3.2.3.2. Finite Element Modelling

The test specimen was fully modeled, including the live- and dead-end anchor blocks by assigning varying thickness to shell elements (see Figure 3.25). In-plane reinforcing bars were modeled as layers of reinforced concrete shell elements. Truss elements were employed for the prestressing tendons and connected to the corresponding shell elements using link elements.

The nodes at the bottom of the live-end anchor block were fully fixed. The circumferential rotational deformations of the nodes at the mid-height of the wall were restrained to prevent unrealistic rotational deformation during the analysis. This rotational deformation is negligible at the low load level. However, throughout the loading steps, it accumulates and potentially leads to unrealistic failure modes. Restraining the rotational deformations improves convergence as well as produces accurate predictions (Choi 2018). Only one node of truss elements at each tendon where the prestressing load is applied was restrained. There was no restraint for other nodes in truss elements. The prestressing load was applied to the nodes at the end of the strands modeled with truss elements in the live-end anchor block as a prescribed displacement.

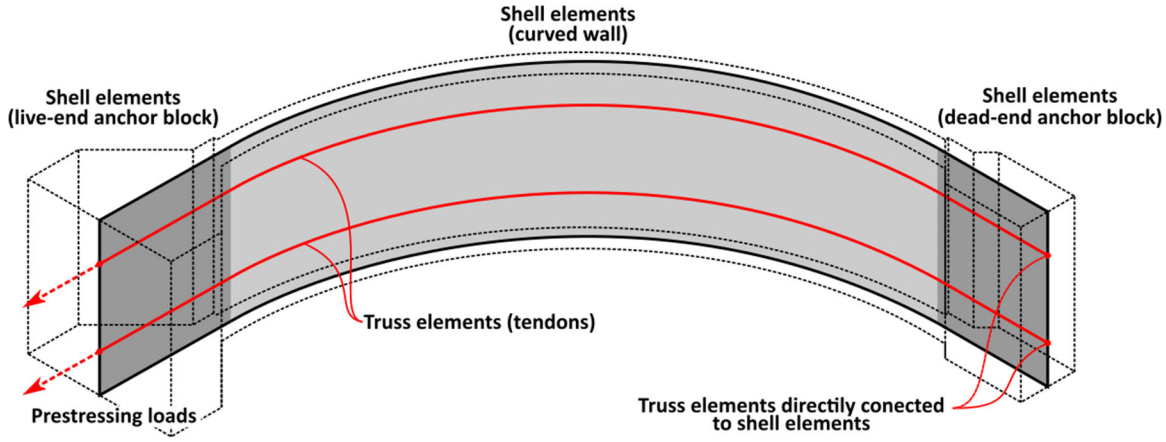

Figure 3.25: Modeling Approach used in VecTor4

Link elements were employed to mimic the behavior of prestressing strands within the ducts (see Figure 3.26). Link elements in the modified VecTor4 are two-noded zero-length elements that can transfer the prestressing forces to the shell elements representing the reinforced concrete wall. The fundamental idea of the link elements is a set of three zero-length truss elements oriented in three orthogonal directions in the local coordinate system. The interaction between concrete and reinforcing bars or prestressing strands can be modeled by defining appropriate stiffness to each zero-length truss in the link element. One of the local coordinate axes of the link element is aligned with the tangential direction of the adjoining truss element representing tendons. By assigning appropriate spring stiffness to the zero-length truss of a link element in a tangential direction, the friction losses along the length of the specimen can be simulated. In contrast, the sprig stiffness of transverse directions needs to have sufficiently large stiffnesses to constraint the truss element and the shell elements. The spring stiffness of a link element aligned in the tangential direction can be obtained on the basis of the conventional friction loss equation in ACI-423 2016 (Choi, 2018; ACI-ASCE Committee 423, 2016).

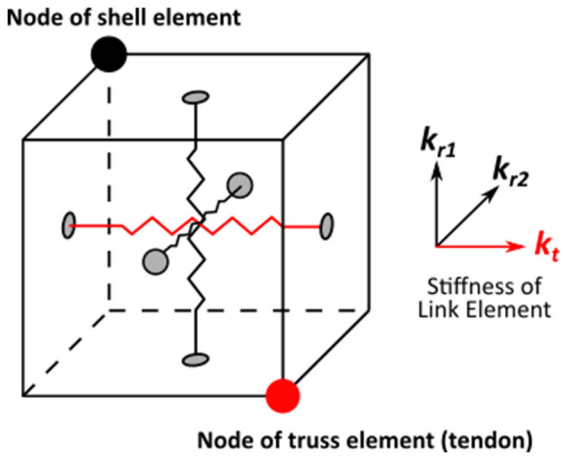

Figure 3.26: Link element (reproduced from Choi, 2018)

The element size and the number of layers in the shell elements were determined based on the mesh sensitivity studies reported by Choi (2018). The curved wall was meshed with 16 elements in its vertical direction and divided into ten elements along the circumferential direction. Each element has 12 layers along its out-of-plane direction of a shell element. The generated mesh is shown in Figure 3.27.

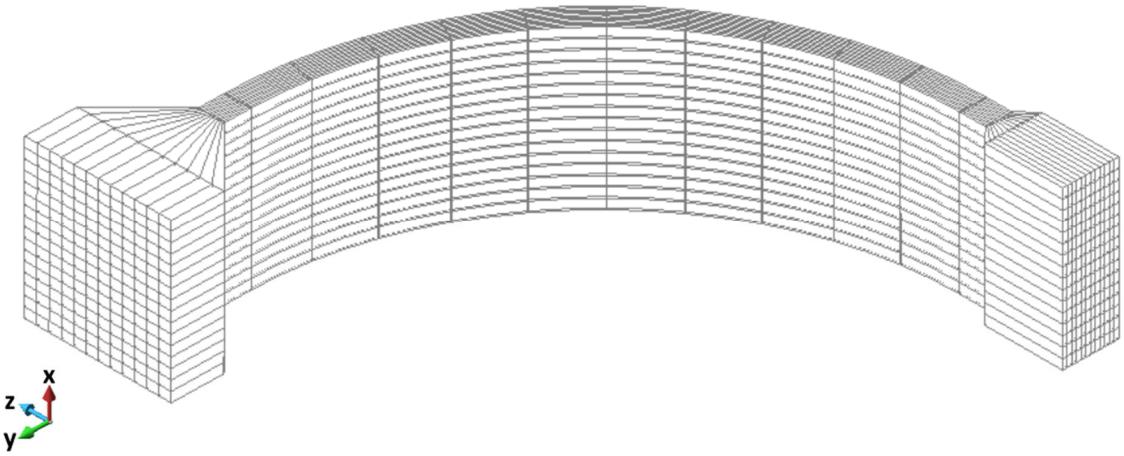

Note: the thickness of layers in shell elements are visualized in the above figure.

Figure 3.27: Generated mesh for VecTor4

3.2.5 Validation: Parameter Investigation

A concrete compressive base curve model may influence the behavior of the specimens before the delamination failure since those structures are subjected to the circumferential compression stress (Choi 2018). Therefore, the influence of the compressive base curve was investigated in this study. Three models for the compressive base curve (Hognestad 1951; Popovics 1973; Thorenfeldt et al. 1987) provided in the VecTor4 program were selected for this study. The Hognestad model (see Equation 3-11) is a parabolic equation that was adopted in the original MCFT. It should be noted that the model of Popovics and Thorenfeldt et al. are referred to as "Popovics (NSC)" and "Popovics (HSC)" in VecTor4, respectively. Both models are expressed as follows.

Popovics (1973)

$$f_c = f_c' \cdot \frac{n \cdot \left(\frac{\epsilon_c}{\epsilon_c'}\right)}{(n-1) + \left(\frac{\epsilon_c}{\epsilon_c'}\right)^n} \qquad \text{Equation 3-14}$$

where, f_c' = Compressive strength of concrete, psi

f_c = Compressive stress at ϵ_c, psi

E_c = Secant modulus; $\mathrm{E_c} = \frac{f_c'}{\epsilon_c'} \cdot \frac{n}{n-1}$

$n = 0.4 \times 10^{-3} f_c' + 1.0$

Thorenfeldt et al. (1987)

$$f_c = f_c{}' \cdot \frac{n \cdot \left(\frac{\epsilon_c}{\epsilon_c'}\right)}{(n-1) + \left(\frac{\epsilon_c}{\epsilon_c'}\right)^{n+k}} \qquad \text{Equation 3-15}$$

where, E_c = Secant modulus; $\mathrm{E_c} = \frac{f_c'}{\epsilon_c'} \cdot \frac{n}{n-1}$

$n = 0.8 + \frac{f_c'}{2500}$

$k = 1.0, \epsilon_c' < \epsilon_c < 0$

$k = 0.67 + \frac{f_p}{9000}, \ \epsilon_c < \epsilon_c'$

Figure 3.28 depicted the compressive base curve of each model used for the current study. One noticeable difference is that the Hognestad model shows slightly higher initial stiffness than other models.

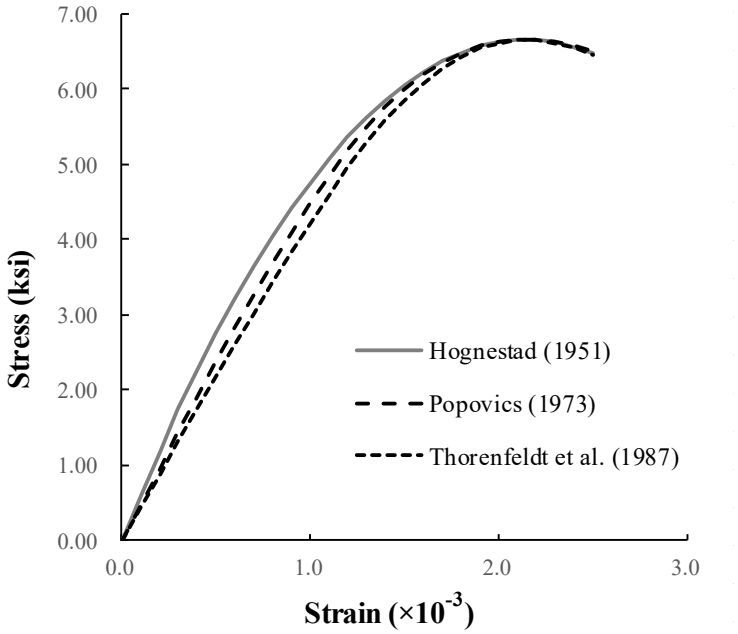

Figure 3.28: Compressive base curve of each model

The analysis results were compared, focusing on the ultimate load and circumferential strains at the locations shown in Figure 2.6. It should be noted that the measured circumferential strain data shown in the figure were averaged over the height of the specimen at each section, and the circumferential strains extracted from the VecTor4 analysis results were also processed similarly.

The estimated ultimate loads with each analysis case are summarized in Table 3.5. It is deemed that the influence of the compressive base curve on the ultimate load prediction is minimal.

Table 3.5: Estimated ultimate load (influence of compressive base curves)

Compressive base curve	Estimated ultimate load kips (kN)	Error* (%)
Hognestad (1951)	1353 (6016)	-7.4
Popovics (1973)	1351 (6011)	-7.5
Thorenfeldt et al. (1987)	1346 (5956)	-7.9

* The ultimate load of the test was 1460 kips (6496 kN)

Figure 3.29 shows the circumferential strains of the inner surface at the 15- and 45-degree locations of the specimen obtained from the actual test and the analyses. The analysis results with Popovics (1973) shows the best agreement with the actual test results. The Hognestad parabola gave a stiffer response than the test results. With Thorenfeldt et al. (1987), the result shows a larger strain than expected.

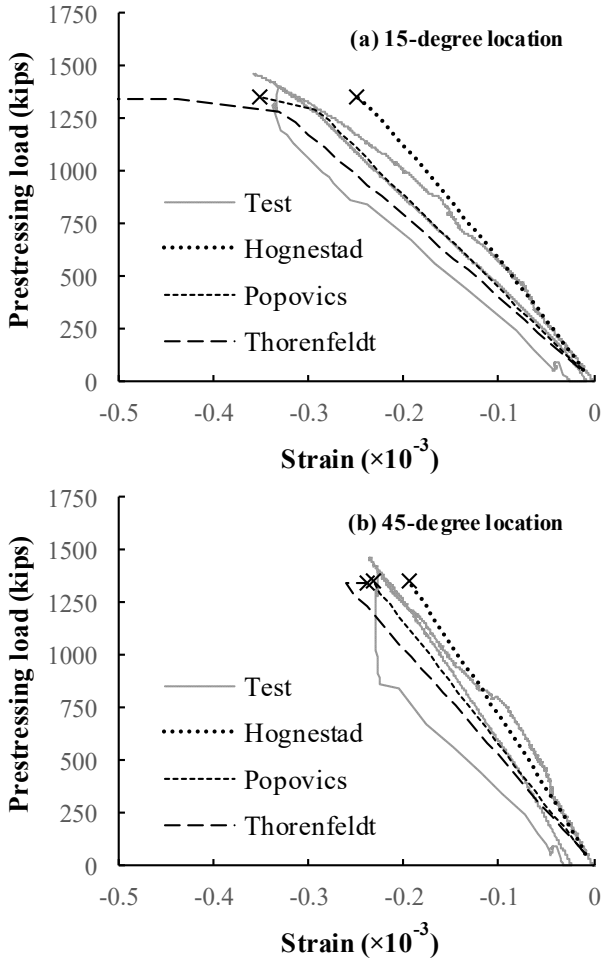

Figure 3.29: Circumferential strain at location of; (a) 15-degree, and (b) 45-degree

Chapter 4. Discussion

This section will discuss the relative merits and limitations of the commercial program Abaqus and the academic program VecTor4 based on the analytical study on the delamination behavior of a recently tested post-tensioned concrete curved wall.

As for the user interface, Abaqus provides a user-friendly graphics-based pre- and post-processor called Abaqus CAE. On the other hand, VecTor4 also has its graphics-based user interfaces called FormWork-plus and Janus as pre- and post-processors, respectively (Wong et al., 2013; Chak and Vecchio, 2013). However, due to the discrepancy between the development of VecTor4 source code and pre- and post-processors, users need to deal with text-based data to some extent. For example, when users want to model the structures with complex geometry in the pre-processor, a text-based input generated by users could be more intuitive and a better option than its pre-processor. To visualize the distribution of arbitrary variables in the manner of contour plot in post-process, users may need other post-process programs than Janus. Since those programs are not typically developed for VecTor4, users may need to interpret the results based on the text-based output files.

The validation analyses with both Abaqus and VecTor4 were conducted. Regarding Abaqus, the appropriate element size, and dilation angle ware investigated. In addition to those parameters, the suitability of the viscosity parameter was also checked. The analysis results imply the program can capture the delamination behavior of post-tensioned concrete curved structures if the parameters are appropriately calibrated. As for the modified VecTor4 program, analysis results show good agreement with the test results obtained from the recent test as well as the previous series of tests on concrete delamination.

Regarding the material models, the CDPM of Abaqus has complicated parameters such as the dilation angle and viscosity parameter. These parameters may have a

considerable impact on analysis results and should be calibrated for each problem. Therefore, the calibration of the CDPM can be challenging. However, Abaqus can be a powerful tool if the calibration data of the similar problems are available. As for VecTor4, the input values required for the program are basic material test results (e.g., cylinder test date, steel coupon test data), and the analysis parameters are automatically calculated within the program. Users only need to choose appropriate behavioral models depending on material properties, loading conditions, and modeling strategies.

The computational cost of Abaqus and VecTor4 are compared by counting degrees of freedom and the number of integration points required to model the entire specimen for the recent test. In general, these numbers have a significant impact on computational cost. With Abaqus, 266,904 degrees of freedom and 147,828 integration points are required if the test specimen is modeled with full-height, including the live-end and dead-end anchor block with the element size of 76.2 mm (3.0 in.) (see Table 4.1). As for VecTor4, the same type of analysis can be achieved with 5,007 degrees of freedom and 19,786 integration points (see Table 4.2). Thus, the required number of degrees of freedom and the integration points in VecTor4 is 1.9 % and 12 % of those numbers required in Abaqus, respectively. Therefore, as expected, the modified VecTor4 can capture the delamination behavior of the test specimen efficiently. When it comes to a system-level analysis, modified VecTor4 could be a powerful tool to efficiently evaluate and assess of delamination behavior.

Table 4.1: Degrees of freedom and number of integration points required for full height models in Abaqus

Element size mm (in.)	Total degrees of freedom	Total number of integration points
1.0 (25.4)	5,641,110	3,497,144
1.5 (38.1)	1,766,910	1,059,742
2.0 (50.8)	411,030	449,104
3.0 (76.2)	266,904	147,828

Table 4.2: Number of integration points required for full-height model in VecTor4

Total degrees of freedom	Total number of integration points
5,007	19,786

Chapter 5. Summary and Conclusion

In the present study, the commercial FEM program Abaqus was selected to evaluate the delamination behavior of the post-tensioned concrete curved wall, and its performance was compared with VecTor4 analysis results. The analysis results of Abaqus shows good agreement with the overall behavior observed in the latest test. The numerical analyses with the modified VecTor4 program, which had already been proved to be a powerful tool for the concrete delamination of the curved walls, were also performed for the recent test. VecTor4 shows reasonably accurate performance for capturing the delamination behavior of the recent test.

The relative merits and limitations of Abaqus and VecTor4 based on the analyses of the recently tested curved post-tensioned concrete structure are summarized in Table 5.1, mainly focusing on their user interface, material models, validity, and computational cost. As for the user interface, Abaqus provides a well-structured pre- and post-processor. VecTor4 also has its graphical-based user interface, but users need to deal with the text-based data to some extent. Regarding the material models for concrete, Abaqus provides the CDPM, which potentially has the capability to capture the behavior of concrete structures subjected to general loading conditions. Still, its calibration may be challenging because some of the parameters of the CDPM are complicated. On the other hand, the behavior of DSFM in VecTor4 can be determined with the parameters obtained from simple and standard material tests. Thus, the user input requirements of the DSFM are much simpler than Abaqus. Abaqus shows excellent performance for the analysis of the delamination behavior of the post-tensioned concrete wall using brick elements. Furthermore, the analysis results with Abaqus implies the possibility to predict the detailed information such as the crack pattern of the specimen. As for the analyses with VecTor4,

those results proved that VecTor4 is an appropriate tool to trace the overall behavior of the wall delamination again. Lastly, the computational costs required to analyze the recent test with each program ware compared. The total degrees of freedom and the number of integration points used in the analyses reveals that the required computational cost with Abaqus tends to be much expensive than that of VecTor4.

For the next step, the additional calibration of the CDPM might be necessary to ensure the accurate delamination behavior predictions in general because the parameters used in this study were only validated based on one test result.

Table 5.1: Relative merits and limitations of Abaqus and VecTor4

	Abaqus R2017x	Modified VecTor4 (Hrynyk, 2013; Choi, 2018)
User interface	• A well-structured graphics-based interface is provided for both pre- and post-process.	• Though the graphics-based pre-processor program FormWorks-plus and the post-process program Janus are available, users basically need to deal with the text-based data to generate models for VecTor4.
Material model	• Abaqus offers two material models for concrete available in its implicit solver. Regarding the CDPM, the model has complicated parameters that need to be calibrated, and the calibration can be challenging.	• The material model for reinforced concrete is based on the DSFM. The parameters governing the DSFM can be defined by the material tests, which makes the calibration simple.
Validity	• The ultimate load can be evaluated appropriately using brick elements and the concrete material model in Abaqus. • Abaqus may capture detailed information such as crack patterns in sections.	• The ultimate load can be evaluated appropriately using the shell elements and the concrete material models in VecTor4.
Computational cost	• The computational cost tends to be more expensive than VecTor4 if the brick elements are adopted.	• Appropriate solutions can be obtained with high computational efficiency owing to the adoption of heterosis type shell elements.

References

Acharya, S., and Menon D. (2003). Prediction of radial stresses due to prestressing in PSC shells. *Nuclear Engineering and Design 2003*, 225(1), 109-125.

ACI Committee 318. (2014). Building Code Requirements for Structural Concrete (ACI 318-14) and Commentary (ACI 318R-14). *American Concrete Institute*, Farmington Hills MI.

ACI-ASCE Committee 423. (2016). 423.10R-16 Guide to Estimating Prestress Losses. *American Concrete Institute*, Farmington Hills MI.

ASME. (2015). 2015 ASME BPVC section III-rules for construction of nuclear facility components-division 2-code for concrete containments (ACI-359-15). *The American Society of Mechanical Engineers*, New York, NY.

Bae, S. (2013). *Radial Tension Induced by Prestressing Forces and Moments. 22th Int. Conf. Struct. Mech. React. Technol.*, International Association for Structural Mechanics in Reactor Technology (IASMiRT), San Francisco, CA.

Basu, P.C., and Gupchup, V.N. (2004). Safety evaluation of rehabilitation of delaminated containment dome. *Nucl Eng Des*, SMiRT 16.

Chak, I. and Vecchio, F.J. (2013). *User's Manual of Janus*, University of Toronto.

Chen, W.F. (1982). *Plasticity in reinforced concrete.* McGraw-Hill Book Company, Maidenhead, UK.

Choi, J., Woods. C.R., Hrynyk, T.D., and Bayrak, O. (2017). Behavior of curved post-tensioned concrete structures without through-thickness reinforcement. *ACI Structural Journal*, 114(4), 983-994

Choi, J. (2018). *Investigating delamination behavior of curved post-tensioned concrete structures.* The University of Texas at Austin.

Choi, J., Woods, C. R., Hrynyk, T. D., and Bayrak, O. (2020). Delamination Cracking Behavior of Curved Post-Tensioned Concrete Structures. *ACI Structural Journal*, 117(3), 169–183.

Choi, J. et al. (2020). Effect of duct spacing on delamination cracking behavior, In preparation.

Comite Euro-International du Beton. (1993). *CEB-FIB-model Code 1990: Design code.* London, Thomas Telford

Dassault Systemes Simulia Corp, (2017). Abaqus, *SIMULIA User Assistance 2017*.

Florida Power and Light Company. (1970). *Turkey Point Unit 3 Containment Dome Report.* Florida Power & Light Company

Florida Power Corporation. (1976). *Crystal River Unit 3 Nuclear Generating Plant - Reactor Building Dome Delamination (Final Report)*.

Genikomsou, A.S. (2015). *Nonlinear Finite Element Analysis of punching shear of reinforced concrete slab-column connections.* The University of Waterloo.

Genikomsou. A.S., and Polak, M.A. (2015). Finite element analysis of punching shear of concrete slabs using damaged plasticity model in ABAQUS. *Engineering Structures*, 98, 38-48.

Herbrand, M., Classen, M., and Hegger, J. (2015). Finite element analysis of post-tensioned continuous prestressed concrete beams under shear loading. *16th European Bridge Conference in Edinburgh, June 2015.*

Hillerborg, A., Modeer, M., and Petersson, P.E. (1976). Analysis of Crack Formation and Crack Growth in Concrete by Means of Fracture Mechanics and Finite Elements. *Cement and Concrete Research vol.6*, 773–782.

Hillerborg, A. (1985). The theoretical basis of a method to determine the fracture energy GF of concrete. *Material and Structures*,18(4):291–6.

Hognestad, E. (1951). *A Study of Combined Bending and Axial* Load *in Reinforced Concrete Members*. University of Illinois.

Hrynyk, T.D. (2013). *Behaviour and modelling of reinforced concrete slabs and shells under static and dynamic loads*. University of Toronto.

Hrynyk, T.D., and Vecchio, F.J. (2015). Capturing out-of-plane shear failures in the analysis of reinforced concrete shells *Journal of Structural Eng*ineering, 141(12), 04015058.

Hrynyk, T.D., Vecchio, F.J. (2017). "Modeling of Reinforced and Fiber-Reinforced Concrete Slabs under Impact Loads," ACI Special Publication, V. 321, pp. 8.1-8.20.

Huang, Y. (2012). *Finite element method for post-tensioned prestressed concrete structures*. University of Oklahoma.

Lee, J., Fenves, G.L. (1998). Plastic-damage model for cyclic loading of concrete structures. *Journal of Engineering Mechanics*., 124(8), 892–900.

Lubliner, J., Oliver, J., Oller, S., and Oñate, E. (1988). A plastic-damage model for concrete. *International Journal of Solids and Structures*, 25(3), 299–326.

NEA-CSNI. (2015). *Bonded or Unbonded Technologies for Nuclear Reactor Prestressed Concrete Containments.* Nuclear Energy Agency of the OECD (NEA).

Popovics, S. (1973). A Numerical Approach to the Complete Stress-Strain Curve of Concrete. *Cement and* Concrete *Research*, 3(5), 583–599.

Selby, R.G., and Vecchio, F.J. (1997). A constitutive model for analysis of reinforced concrete solids. *Canadian Journal of Civil Engineering*, 24,460-470

Souza Neto, E.A., Peric, D., and Owen, D.R.J. (2008). *Computational methods for plasticity: Theory and applications*. John Wiley & Sons Ltd., ISBN: 978-0-470-69452-7.

Thorenfeldt, E., Tomaszewicz, A., and Jensen, J. J. (1987). Mechanical Properties of High-Strength Concrete and Application in Design. *Proceeding of the Symposium on Utilization of High-Strength Concrete*, Tapir, Trondheim, 149–159.

Vecchio, F.J., and Collins, M.P. (1986). The modified compression-field theory for reinforced concrete elements subjected to shear. *ACI Journal*, 83(2) 219–231.

Vecchio, F.J., and Selby, R.G. (1991). Toward compression-field analysis of reinforced concrete solid. *Journal of Structural Eng*ineering, 117(6), 1740-1758.

Vecchio, F.J. (2000). Disturbed stress field model for reinforced concrete: Formulation. *Journal of Structural Engineering*, 126(9), 1070-1077.

Vecchio, F.J. (2001). Disturbed stress field model for reinforced concrete: Implementation. *Journal of Structural Engineering*; 119(12), 3590-3610.

Wahalathantri, B.L., Thambiratnam, D.P., Chan, T.H.T, and Fawsia, S. (2011). A material model for flexural crack simulation in reinforced concrete elements using Abaqus. In Proceedings of the First International Conference on Engineering, *Designing and Developing the Built Environment for Sustainable Wellbeing*, Queensland University of Technology, Brisbane, Qld, 260-264.

Wang, S., and Munshi, J.A. (2012). Design of radial reinforcement for prestressed concrete containments. *Nuclear Engineering and Design*, 255:153–61.

Wang, S., and Munshi, J.A. (2013). Repair of Delaminated Prestressed Concrete Cylinders using Post-Installed Anchors: Part I – Radial Tension Demand and FEM Analysis. *22th Int. Conf. Struct. Mech. React. Technol*. International Association for Structural Mechanics in Reactor Technology (IASMiRT)

Wosatko, A., Winnicki, A., Polak, M.A., and Pamin, J. (2019). Role of dilatancy angle in plasticity-based models of concrete. *Archives of Civil and Mechanical Engineering*, 19(4), 1268-1283

Wong, P.S., Vecchio., F.J., and Trommels, H. (2013). *VecTor2 & FormWorks User's Manual Second edition*. University of Toronto.

Yapar, O., Basu, P.K., and Nordendale, N. (2015). Accurate finite element modeling of pretensioned prestressed concrete beams. *Engineering Structures*, 101,163-178